EMBEDDED ULTRASONIC INSPECTION OF LIQUID FILLED PRESSURE VESSELS

by

Trevor Wenzel

A Thesis Submitted in

Partial Fulfillment of the

Requirements for the Degree of

Master of Science

in Engineering

at

The University of Wisconsin-Milwaukee

August 2023

ABSTRACT

EMBEDDED ULTRASONIC INSPECTION OF LIQUID FILLED PRESSURE VESSELS

by

Trevor Wenzel

The University of Wisconsin-Milwaukee, 2023
Under the Supervision of Professor Nathan Salowitz

Structural health monitoring and ultrasonic inspection techniques can be used to inspect a structure for degradation. There are several different approaches for doing this including the use of an embedded sensing system which uses elastic wave propagation through the structure. Previous work using this method has explored ultrasonic inspection of a simple, flat plate structure, however, structures often have more complex geometry, and the flat plate offers only a basic understanding of elastic wave propagation. Therefore, experimental approaches and results drive how these techniques can be used for ultrasonic inspection of complex vessels where challenges arise due to the potential for multiple elastic wave propagation modes and paths through the complex geometry combined with effects of changing environment conditions.

Research here investigates the fundamental capability of using embedded ultrasonic inspection techniques on a complex pressurized water tank structure using the previously established methods for basic structures. The investigation uses permanently mounted lead zirconate titanate piezoelectric transducers to actuate and sense ultrasonic waves propagating through the tank structure. The change in wave propagation is explored through the simulated damage of a magnet placed on the structure, filling the tank, and pressurizing the tank. The results of this work are intended to provide a basis and physics-based understanding upon which to build

capabilities of structural health monitoring of liquid filled pressure vessels to detect and locate degradation under different environmental and state effects.

Liquid filled pressure vessels are common in modern life, from the water heaters in our homes to the fuselage of a spacecraft. Failure of liquid filled pressure vessels can have severe consequences resulting in direct damage due to liquid release, as well as the consequences of system failure and downtime. Therefore, the use of structural health monitoring based on embedded ultrasonic systems has the potential to significantly impact the safety and reliability of a system and to save resources spent in maintenance and downtime with its ability to detect, locate, characterize, and quantify degradation of a structure.

Dedicated to my family and friends who have supported me on this journey.

TABLE OF CONTENTS

LIST OF FIGURES

LIST OF ABBREVIATIONS

SHM	Structural Health Monitoring
PZT	Lead zirconate titanate piezoelectric transducer
NASA	National Aeronautics and Space Administration
SMIS	Shuttle modal inspection system
NDT/E	Nondestructive testing / evaluation
EMI	Electromechanical impedance
PCC	Pearson correlation coefficient
NSE	Normalized signal energy
Cov	Covariance
f-d	Frequency-thickness
MHz	Megahertz
mm	Millimeters
m/s	Meters per second
RMSD	Root mean squared deviation
MAPD	Mean average percentage deviation
CCD	Correlation coefficient deviation
psi	Pressure per square inch
ToF	Time of flight

ACKNOWLEDGEMENTS

I would like to express my sincere gratitude to my thesis advisor, Professor Nathan Salowitz, and research partner, Jomah Mohammad Eyadeh Alzoubi, for their guidance, support, and encouragement throughout the entire research process. Their expert advice and help have been invaluable in shaping the direction of this study. I would also like to thank the faculty and staff of the UWM College of Engineering and Applied Science for their unwavering support and for providing me with a conducive environment to pursue my research interests. I am also grateful to my family and friends for their constant encouragement, motivation, and support, both emotionally and financially, which enabled me to complete this project. Their unwavering belief in me has been a constant source of strength and inspiration. Finally, I would like to thank the project sponsors with the Wisconsin Space Grant Consortium, AMCE Products, and A.O. Smith for providing financial support and resources for this study. Their investment in this research has enabled me to pursue my academic goals and make a valuable contribution to the field. Thank you all for your support and encouragement. This thesis would not have been possible without each and every one of you.

Chapter 1 Introduction

Damage detection is important in almost all engineering fields and disciplines for creating life-safe environments and can provide large cost savings for business. Structural health monitoring (SHM) and ultrasonic inspection techniques have been developed for such damage detection. The application of these techniques has faced many challenges in creating effective feature selection to differentiate damage and non-damaged states of the system. Here is an overview on the use of SHM and ultrasonic sensing as well as case studies of the use of embedded lead zirconate titanate piezoelectric transducers (PZTs) in laminate beam defect identification and wireless aircraft wing SHM.

1.1 Use of Structural Health Monitoring

Structural health monitoring has been around for many years as a way to detect damage in a system that could lead to failure of the system and has common applications across multiple engineering disciplines including aerospace [1], mechanical [2], civil [3], and electrical engineering [4]. Our aim is to create an embedded and automated monitoring system that compares the current state to the initial (undamaged) state. Damage can occur in the material due to natural wear over the life of the system or unexpected high stress past the system design intent and it can cause the material to perform at suboptimal levels. SHM will provide damage detection using measurements of the system to analyze the integrity of the system. This is especially useful because it allows for almost immediate feedback on the system state in the event of an extreme stress condition [5].

1.1.2 Range of SHM Application

SHM applications range across a variety of both private business and public government sectors for the potential impact in terms of safety and real dollar savings. There are a multitude of examples of the need for SHM in different applications. This includes semiconductor manufacturing where redundant machinery in used to avoid potential downtime from machinery breaking and SHM can eliminate additional machinery by predictive analysis of the machinery condition. Damage detection could be used on aerospace structures that have small design margins and can accumulate fatigue damage under cyclic loading [6]. Key infrastructure that is exceeding the designed life and has significant accumulated damage from years of use and could be monitored to prevent major problems if they fail unexpectedly [7]. Lastly, another widespread application for the use of SHM is in time-based maintenance of structural or mechanical systems where a system is phased out of active use after a predetermined set of duty cycles [8]. While there is a large statistical basis for time-based approach that is based on test data and finding reliability of the components, it could be further optimized using SHM to provide real time performance status of the system components and offer more insight to extend the life of the system and provide the business with monetary savings [9].

1.1.3 Historical Use of SHM

In the most basic sense, damage detection techniques have been used for centuries dating back to any process to test the integrity of a structural system in a nondestructive test. Modern advancement of what is known as SHM today is possible because of the large-scale advancement in digital computing and its capabilities to adapt to different uses. Three key industries of oil, aerospace, and civil infrastructure pushed the large-scale advancement of SHM

in the United States of America in the 1970s and 1980s. Big oil companies pushed for SHM advancement specifically for damage identification for offshore oil harvesting applications where high stress results from large vibrations of machinery. This application is unique in that damage can occur across a large range of locations that are not readily accessible to measure. Techniques were developed to solve this using numerical modeling and analysis of resonance frequencies in simulated damage conditions and correlate to the real system. Aerospace began using SHM technology in the product development of the space shuttle which experienced similar need for damage detection in high stress conditions due to vibration of machinery [9]. The National Aeronautics and Space Administration (NASA) developed the shuttle modal inspection system (SMIS) to look at critical areas of the shuttle blocked by protective heat shielding that prevents ease of access [10]. NASA uses these damage detection tools and analysis techniques on other space projects as well including testing orbiter vehicles, structural components of space stations, and reusable launch vehicles. Civil structures use damage assessment across bridge and building structures with unique environment and operating conditions. Techniques for the analysis of damage involve dynamic flexible matrix indices and shape curvature for the unique structures seen in this application and allow for ease of inspection of the structure which is often required from a regulatory standpoint [11].

1.1.4 Statistical Pattern Recognition Paradigm

A method used to breakdown and categorize the SHM process is the four steps of the statistical pattern recognition paradigm. The steps are operational evaluation, data processing (acquisition, normalization, and cleansing), feature selection and information condensing, and statistical model development for feature discrimination. The first, operational evaluation,

looks at the conditions of the damage identification use case. This starts with a definition of the motivation for SHM use whether it is life-safety, monetary gain, or a combination of both and the definition of what is considered as damage and how to categorize it. Then, the operating conditions are explored and limitations to monitoring capability defined to create an effective SHM system for the application desired. Next is the phase of data acquisition, normalization, and cleansing which is the technical setup of the SHM system including all the specifics of how the data is collected. Once collected, the data must also be processed to create a baseline condition to normalize all data taken out of the standard control conditions and environment so it can be compared in the analysis of the system in the next phase. Another portion of the data refinement is cleansing the obtained data to eliminate non useful data taken when other factors affected the sensor outputs that do not mean the system has undergone actual damage. The third phase of this process is feature selection and information condensing in which both damaged and nondamaged condition are defined. The most basic technique used is to correlate the system response values obtained in data collection with observation of the system and tracking damage accumulation. Other methods involve inducing damage to the system that is expected in the actual use case to analyze the response of the system. This may involve using different induced damage types in testing like fatigue, corrosion, or temperature to analysis system response and find which is most appropriate for the desired application. Finally, the final step in structural health monitoring is to create a robust statistical model to distinguish the damaged state of the system from an undamaged and normal operating system. If there is a multitude of data collected for each state, supervised learning techniques like group classification are used where objects are grouped based on a commonality. In this case it would

be either the damaged or undamaged states that are classified by groups. Regression analysis is another technique where damage accumulation is tracked over the life of the system. If there is inadequate data for analysis using these techniques, then unsupervised learning may be used to detect damage when there is an outlier in the data that suggests a change in the state of the system. When damage is found, it must also be analyzed based on the location, type, and severity to predict expected life of the system. With either technique, there exists the possibility of error in damage detection whether it is sensing damage that is not present (false positive) or unable to detect damage that has occurred (false negative). The model must be adjusted with this in mind to create a robust model to reduce the possibility of failure of the system [9, 12, 13, 14].

1.1.5 Challenges Using SHM

SHM relies on a change in the condition of the system that is both measurable and will change the measured response of the system. This has been a large challenge as damage often occurs on a small area and may not have a measurable response on the system as a whole. The damage could also occur as a result of varying modes and magnitude depending on the environment and operating conditions and issues occur measuring damage in these often-rough conditions. Challenges can result in attempts to create the appropriate analysis when the damage experienced is unknown beforehand. In this case, the model for analysis relies on the unsupervised learning techniques to find the outlier in the data measured. Another challenge SHM faces is reliability of the monitoring sensor systems where sensor damage itself can cause large issues in the network and prevent accurate damage detection of the system [9, 15, 16].

1.1.6 Summary of SHM

SHM has been around for many years as a method to detect damage of a system and monitor performance. Applications where SHM could be implemented range over many different fields from the monitoring of a control system of a space shuttle to preventing downtime of machinery in an industrial plant. Historically, large and influential industries like oil and aerospace have led the research in this field, but now a variety of unique applications make this an up and coming research area. The statistical pattern recognition paradigm describes how SHM is used and applied in the most basic sense to different applications with how data is collected and processed. SHM does have issues to resolve when it comes to this damage detection as there are so many unknowns that come into play in complicated systems, however, continued research will provide more clarity and refinement of these techniques.

1.2 Damage Detection in Laminate Beam Application

Laminate structures often use ultrasonic non-destructive testing and evaluation (NDT/E) for damage detection, but a large challenge has been feature selection and discrimination between an undamaged and damaged bond condition [17]. A variety of techniques have been researched including ultrasonic C-scan [18, 19, 20, 21, 22, 23, 24], shear waves [18] and antisymmetric Lamb waves [19], and wedge ultrasonic transducers [20] in an attempt to create effective methods to differentiate bond states. Another common technique used is electromechanical impedance (EMI) where embedded PZTs placed on the structure [25, 26]. An electronic signal is applied to one PZT and the other PZTs on the structure measure the resulting mechanical vibration of the structure [27]. Differences in this response can be used to categorize and locate degradation in the structure [28]. The application of this technique is

dependent on the structure being analyzed, but lessons can be learned by seeing how it was used on a simple structure to explore how it may be applied to more complex structures like a pressure vessel. One experiment was done with a laminate beam employing this method using ultrasonic waves and embedded sensors with the pitch-catch configuration. From this setup, EMI analysis techniques were used for monitoring the transducers in the three-point bending test to examine bond strength and damage detection. Discussed are the results of this study and how this will impact future damage detection techniques and research. **Figures 1.1** and **1.2** below show an overview of the experiment setup and laminate test object during testing and **Figure 1.3** shows a flowchart of the operating principles of the experiment [29].

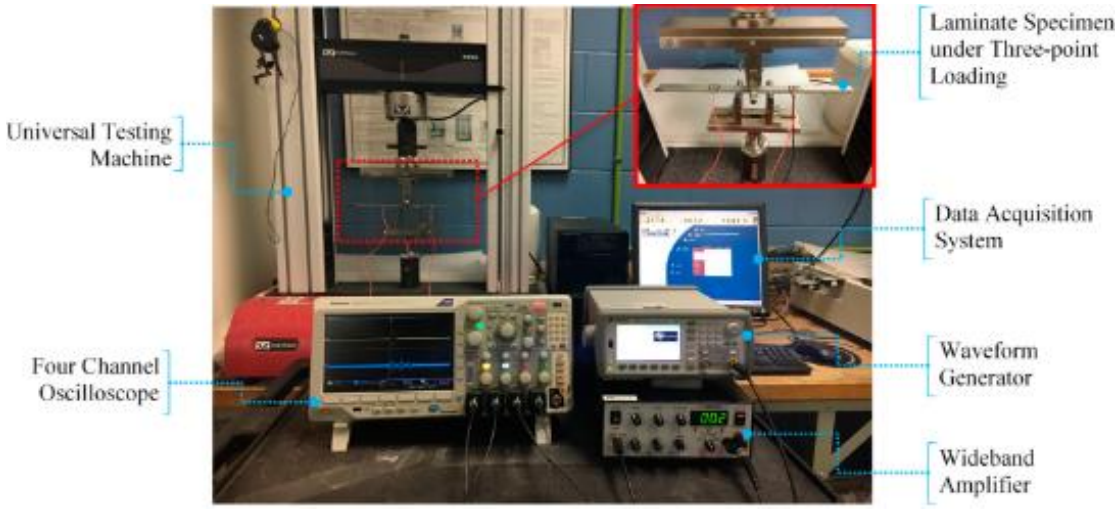

Figure 1.1 Experimental setup used in three-point bending test [29].

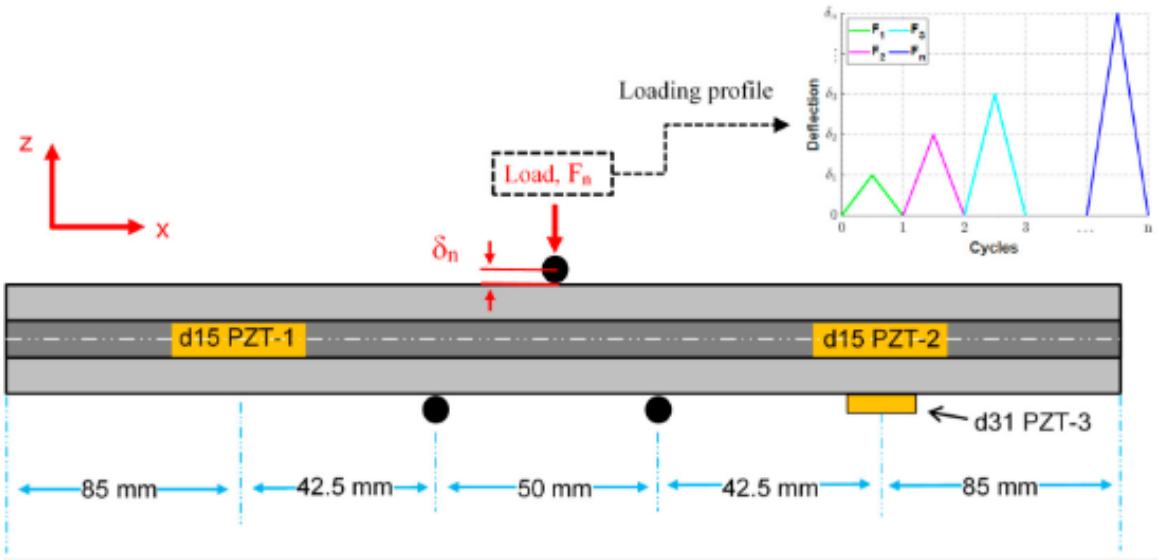

Figure 1.2: Laminate object under three-point bending in experiment [29].

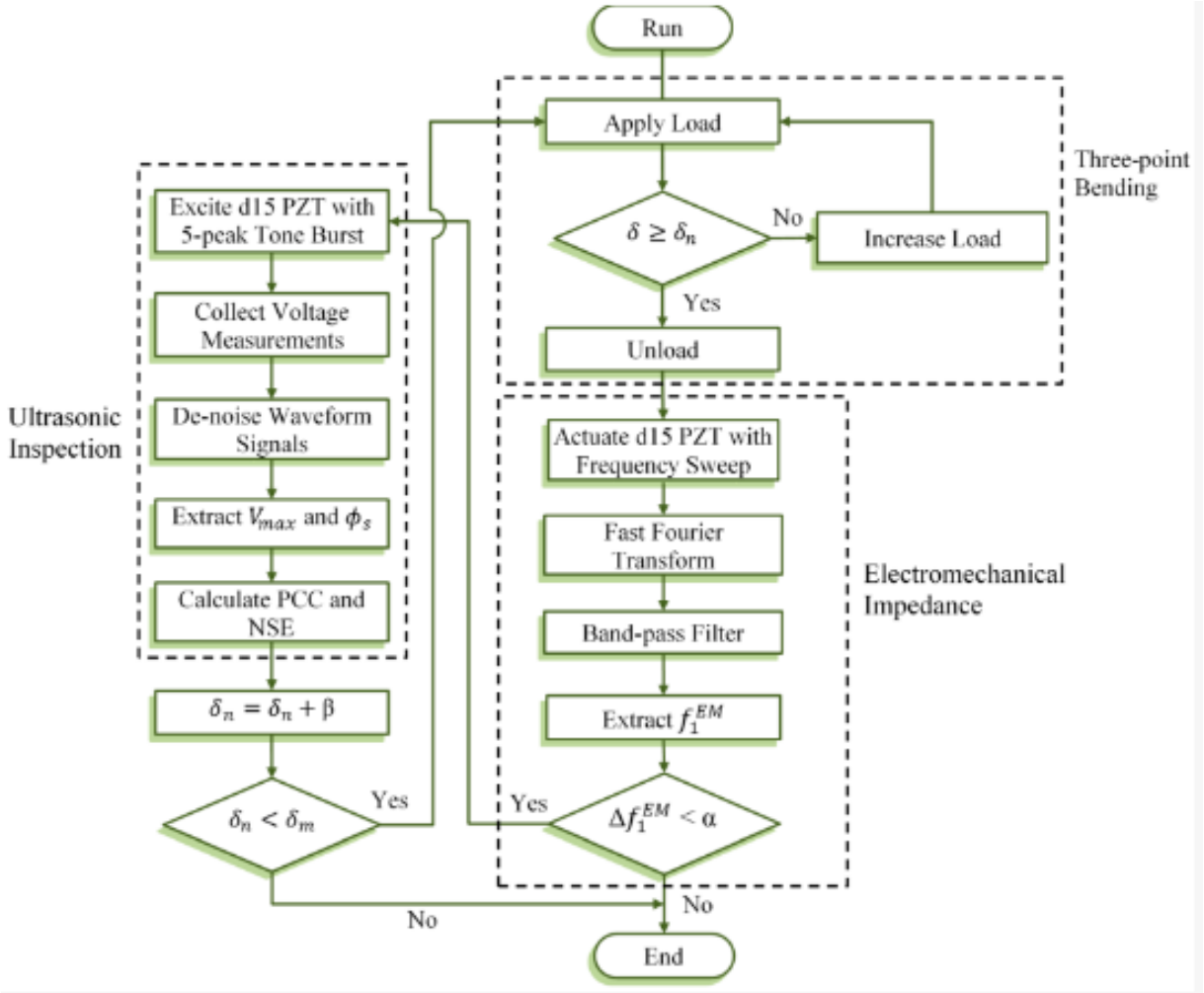

Figure 1.3: Flowchart for experimental setup of ultrasonic inspection of transducers during three-point bending test [29].

1.2.1 Experiment Results and Discussion

There are multiple sections of this research including the ultrasonic inspection, three-point bending, and electromechanical impedance. Specifically of interest is the use of ultrasonic inspection and how it uses the pitch catch configuration of embedded and surface mounted PZTs with a five-peak actuation signal with a center frequency of 30 kHz. Trials were done actuating the signal from PZT-1 to PZT-2 as well PZT-1 to PZT-3 locations as described in Figure 1.2 at both 1 mm and 3.3 mm mid-span deflections [29]. The results are shown below in **Figures 1.4-1.7**.

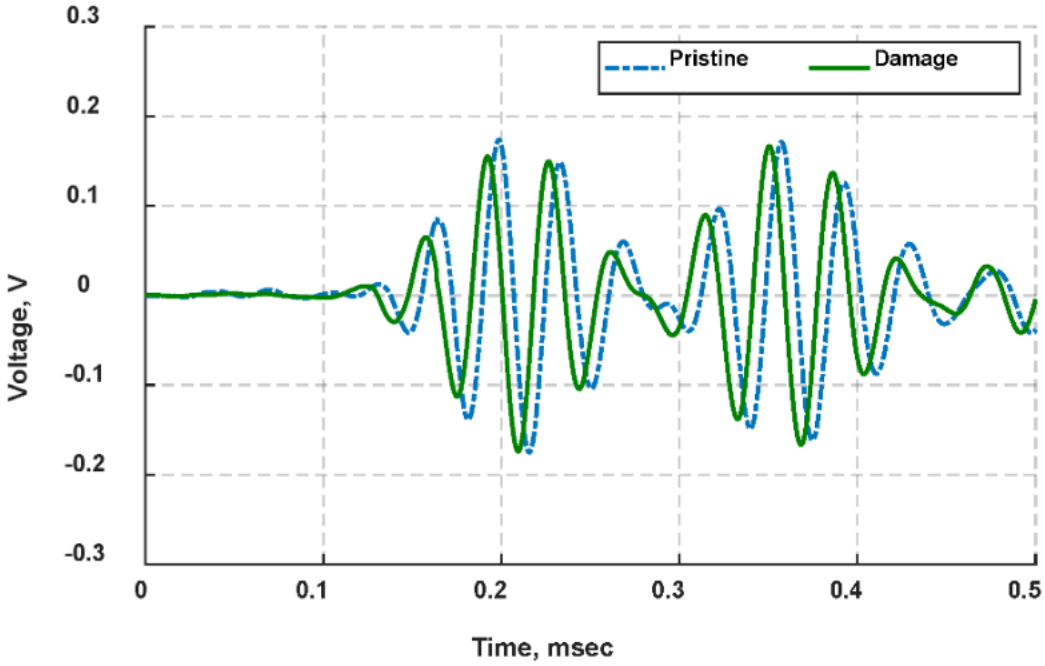

Figure 1.4: Comparison of waveform signals collected from bondline-embedded d15 PZT and surface mounted d31 PZT sensors at 1 mm deflection (PZT-1 to PZT-2) [29].

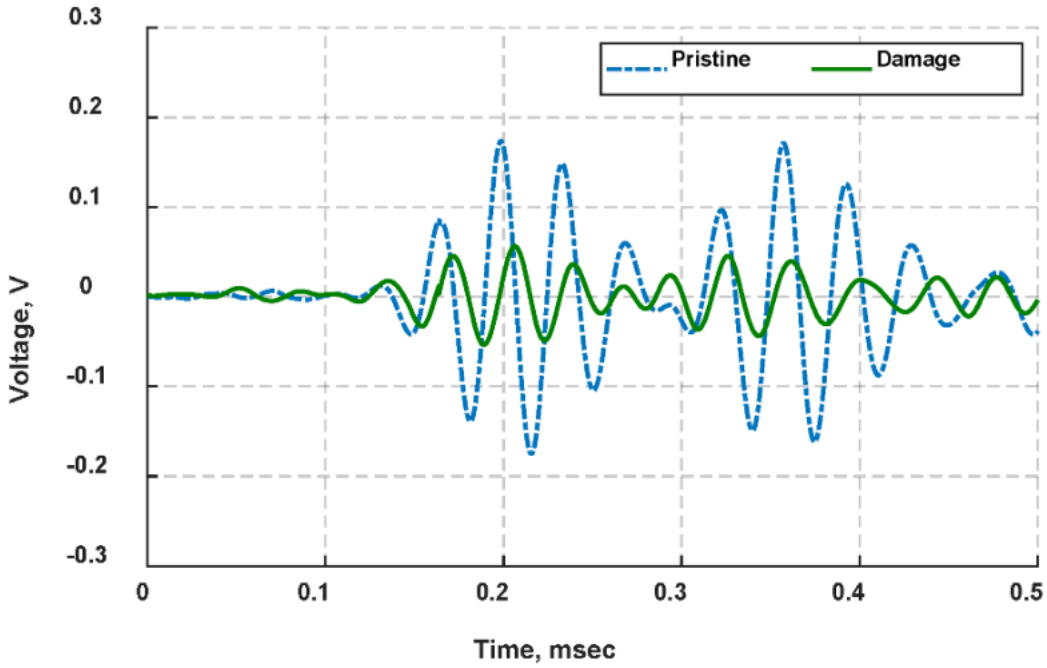

Figure 1.5: Comparison of waveform signals collected from bondline-embedded d15 PZT and surface mounted d31 PZT sensors at 3.3 mm deflection (PZT-1 to PZT-2) [29].

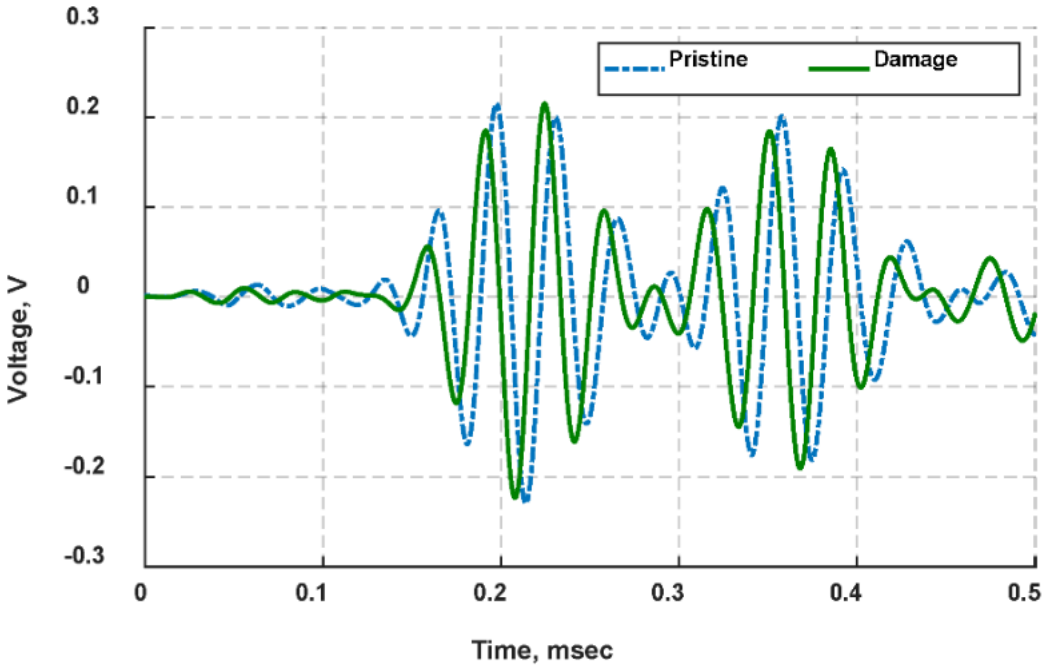

Figure 1.6: Comparison of waveform signals collected from bondline-embedded d15 PZT and surface mounted d31 PZT sensors at 1 mm deflection (PZT-1 to PZT-3) [29].

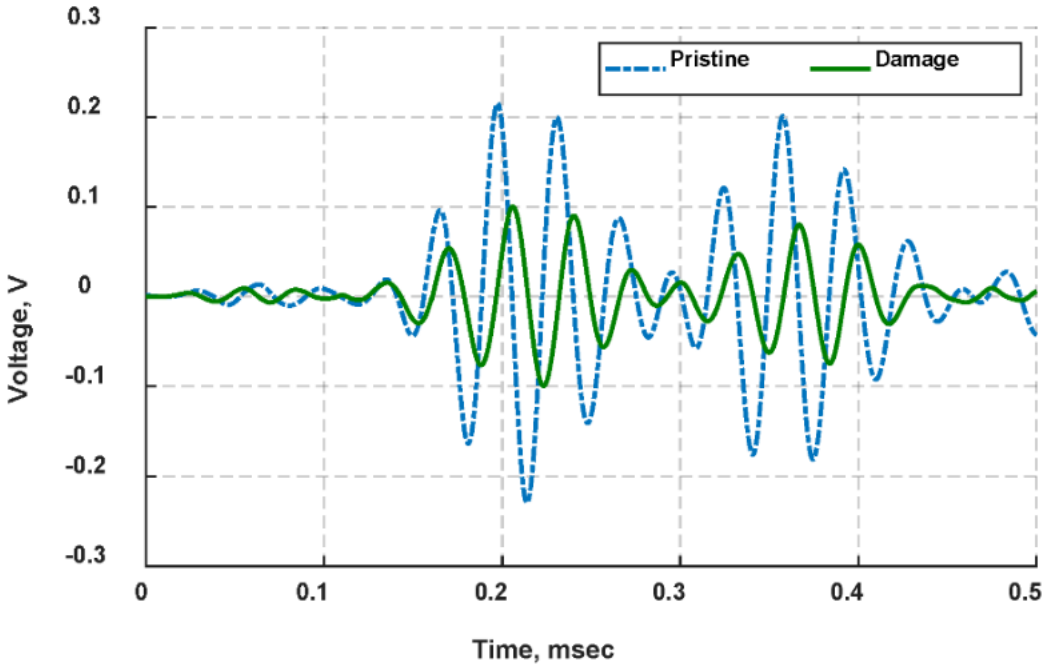

Figure 1.7: Comparison of waveform signals collected from bondline-embedded d15 PZT and surface mounted d31 PZT sensors at 3.3 mm deflection (PZT-1 to PZT-3) [29].

Pearson correlation coefficient (PCC) and Normalized Signal Energy (NSE) were used and compared with the damage state throughout and are defined below in **Figure 1.8**.

$$cov(X,x) = \frac{1}{N}\sum_{i=1}^{N}\left(X_i - \overline{X}\right)(x_i - \bar{x})$$

$$PCC = \frac{cov(X,x)}{\sigma_X \sigma_x}$$

$$NSE = \frac{\sum_{i=1}^{N} X_i^2 - \sum_{i=1}^{N} x_i^2}{\sum_{i=1}^{N} X_i^2}$$

Figure 1.8 Covariance (cov), PCC, and NSE definition [29].

The cov is secondary calculation used in the calculation of the PCC and uses the *i*th measurement point X_i and x_i of the undamaged waveform and comparison signal values, respectively. It also uses the number of measurements, *N*, and mean values, $\bar{X}$ and $\bar{x}$, of the undamaged waveform and comparison signal, respectively. The PCC uses this covariance calculation and divides by the standard deviation of the undamaged waveform and comparison signal, σ_X and σ_x, respectively. The NSE uses the *i*th measurement point X_i and x_i of the undamaged waveform and comparison signal values, respectively, and number of measurements, *N*, as well. In this study, the damage index related to the PCC calculation was calculated as 1 – PCC to provide consistency in the analysis and comparison of the two [29].

The PCC damage index increases with increasing deflection until the start of the major transition at 1 mm. where the crack in the structure is fully developed. Then, the PCC decreases greatly as the deflection continues to increase until the end of the major transition at 2.3 mm. Finally, the PCC increases sharply reaching its maximum value at the end of the test at 3.3mm of deflection. The NSE damage index, however, experiences only a minor decrease as the deflection increases from 0 to 2.3mm. Then, it sharply increases along as was seen with the PCC from 2.3 to 3.3 mm. of deflection. Below in **Figure 1.9-1.11** the results are shown graphically with the three trials using d15 PZT-2, d31 PZT-1, and d15 PZT-1.

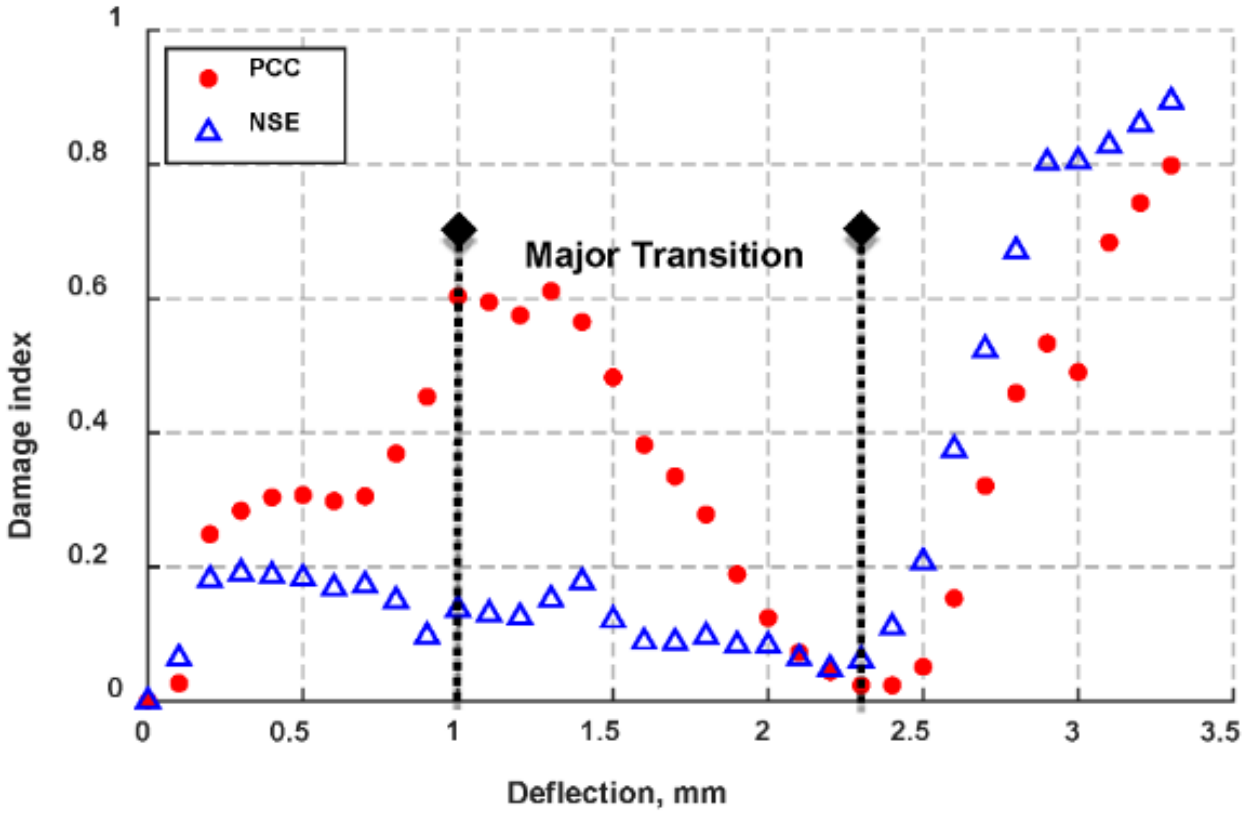

Figure 1.9: Damage index values based on Pearson correlation coefficient and normalized signal energy methods calculated for the first arrival of sensor signals received by d15 PZT-2 [29].

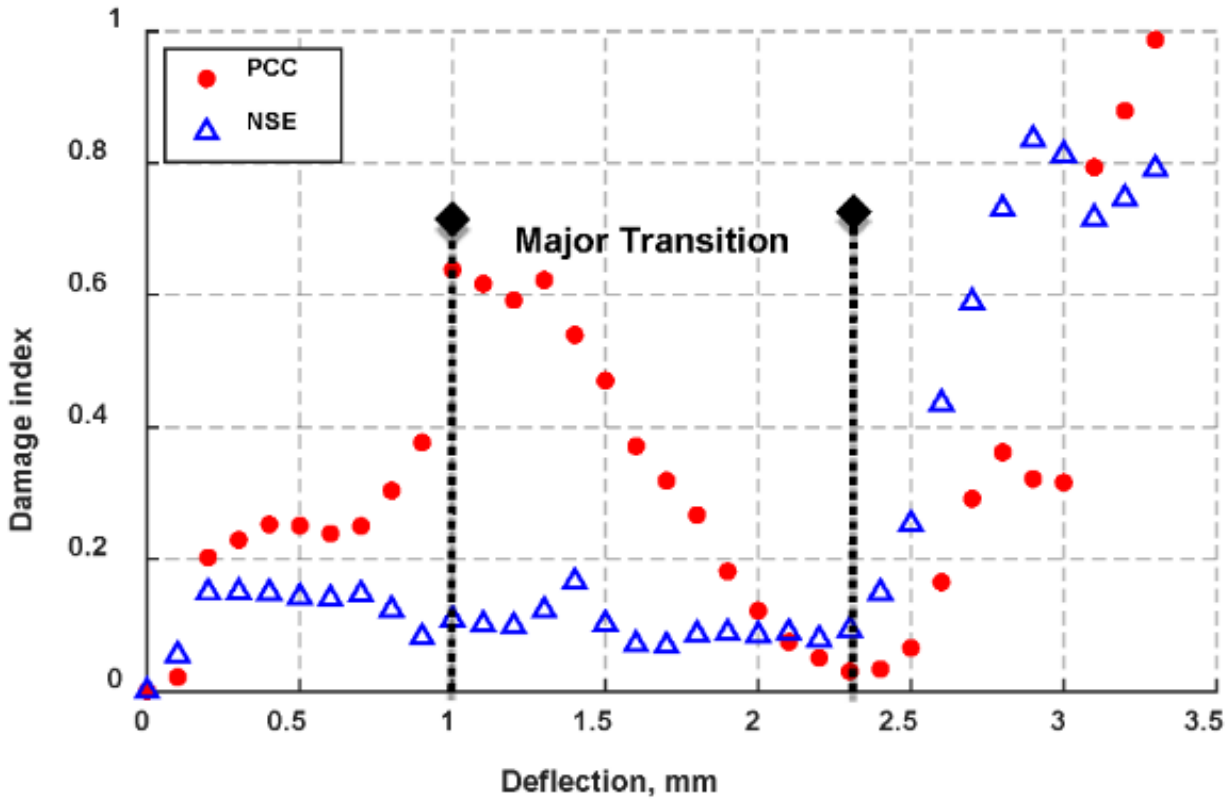

Figure 1.10: Damage index values based on Pearson correlation coefficient and normalized signal energy methods calculated for the first arrival of sensor signals received by d31 PZT-3 [29].

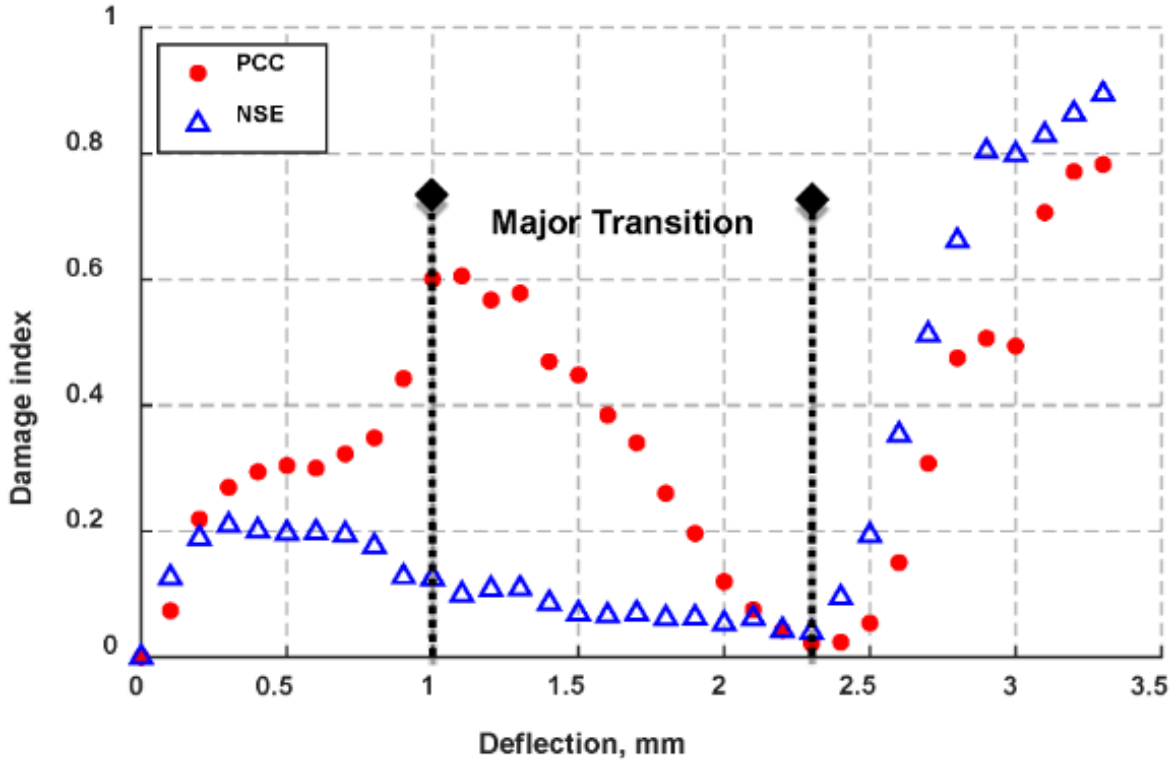

Figure 1.11: Damage index values based on Pearson correlation coefficient and normalized signal energy methods calculated for the first arrival of sensor signals received by d15 PZT-1 [29].

From the results, it was found that the PCC damage index is more sensitive to phase shift while the NSE damage index was more sensitive to the voltage amplitude of the signal [29].

1.2.2 Summary of Laminate Beam Deflection Study

The research conducted in ultrasonic inspection of laminate beam undergoing a three-point bending test provided insight to how the PZTs can be used in a damage detection application. Further work still is needed to continue the work with this methodology, but the initial results show promise in the PZT's ability to detect damage. This research shows that this method is capable of more in-depth damage detection that could include identification of magnitude and

location of damage. Application of this technique will look to explore how this can be used to find the characteristics of the damage including severity and useful life of the system.

1.3 Embedded Ultrasonic in Beams and Plates

Another study that investigates the use of embedded PZTs for damage detection is one done on composite plates [30]. The study uses a clock-like sensor array as shown in **Figure 1.12** below to test the capability of the sensor network to detect damage with this array vs the traditional distributed array of sensors as shown in **Figure 1.13.**

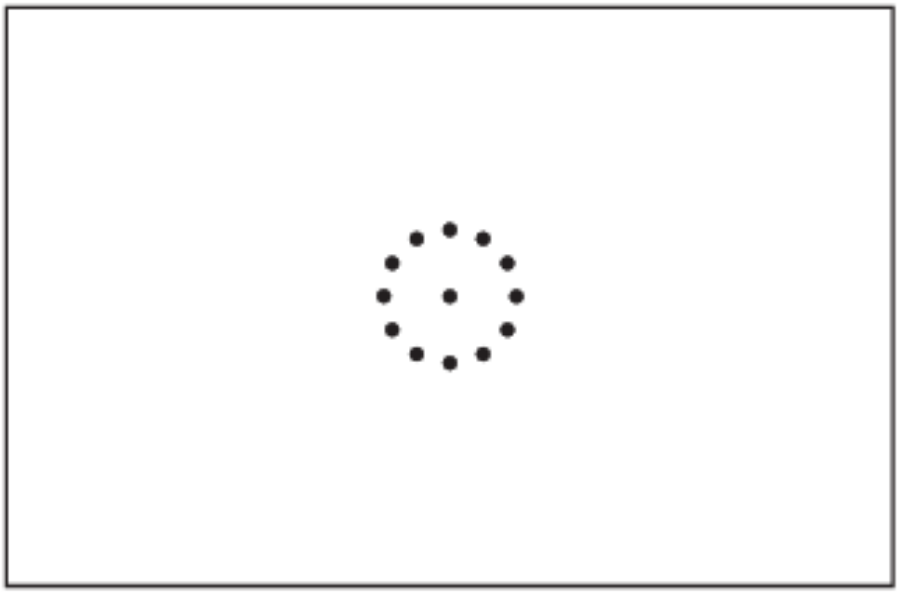

Figure 1.12 Circle-like sensor array [30].

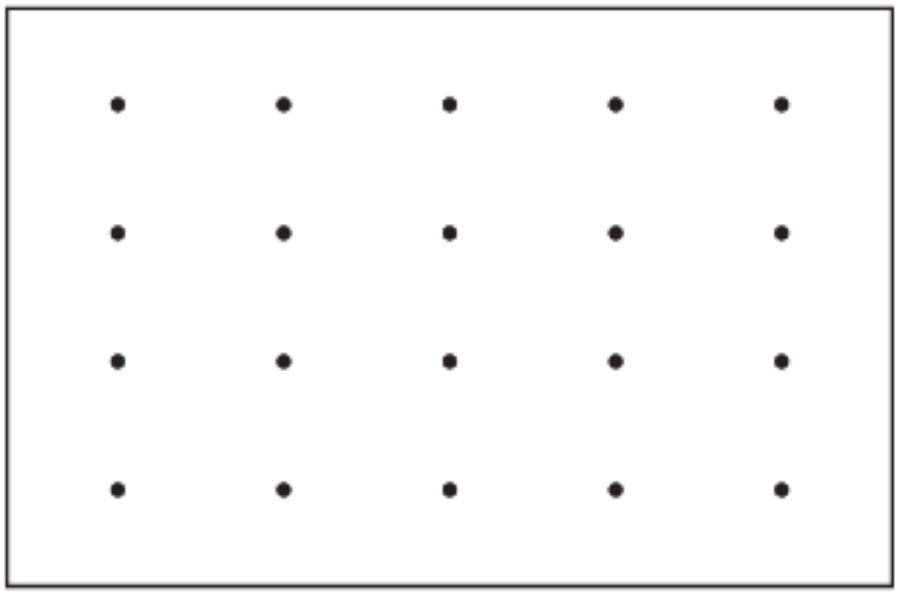

Figure 1.13 Dispersed sensor array [30].

This work uses a similar approach as discussed previously with an input signal actuated by the center PZT. The surrounding PZTs are used to sense the excited Lamb waves which propagate primarily through the antisymmetric and symmetric modes though the structure.

The test specimen used in this experiment is a composite plate 2 millimeters thick with two cracks with the sensor array placed as shown in **Figure 1.14** below.

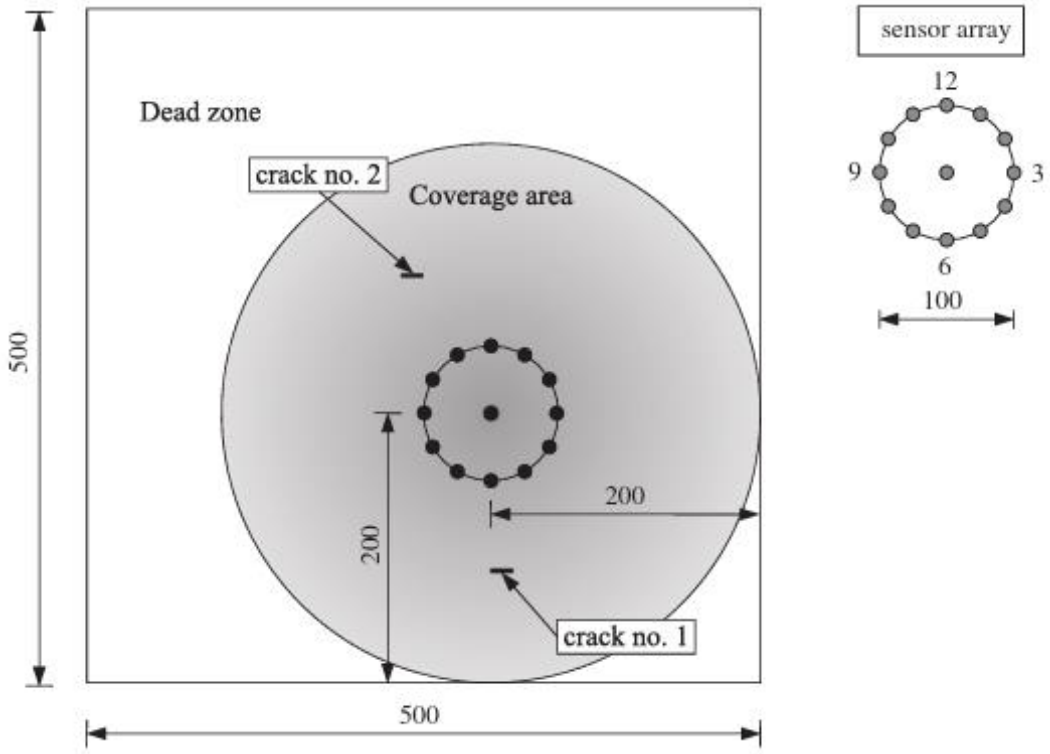

Figure 1.14 Composite plate geometry with circle-like sensor array and two cracks located on the structure [30].

The results of this ultrasonic inspection are shown at different time intervals of 0.07, 0.12, 0.16, and 0.21 milliseconds in **Figures 1.15-1.18** below.

Figure 1.15 Propagating wave in composite plate at 0.07 milliseconds [30].

Figure 1.16 Propagating wave in composite plate at 0.12 milliseconds [30].

Figure 1.17 Propagating wave in composite plate at 0.16 milliseconds [30].

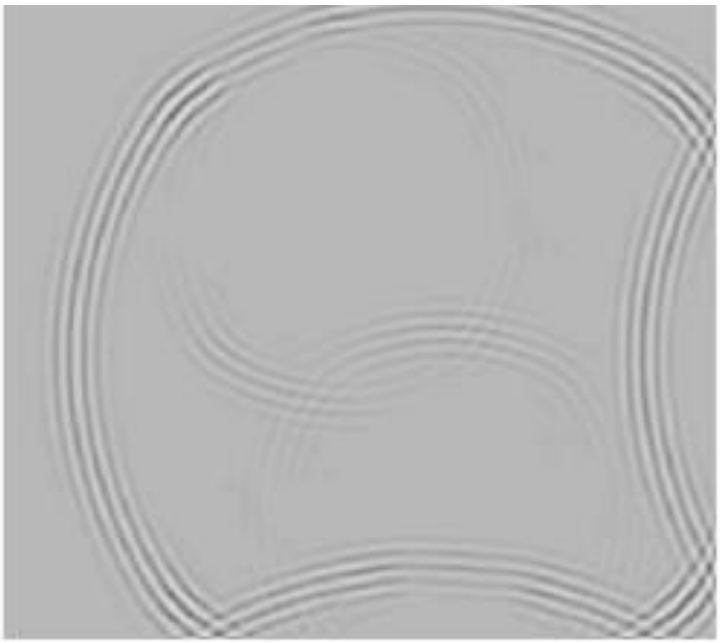

Figure 1.18 Propagating wave in composite plate at 0.21 milliseconds [30].

The numerical results were then mapped using a damage influence map to show the effectiveness of removing boundary conditions and having a baseline established as shown below in **Figure 1.19.**

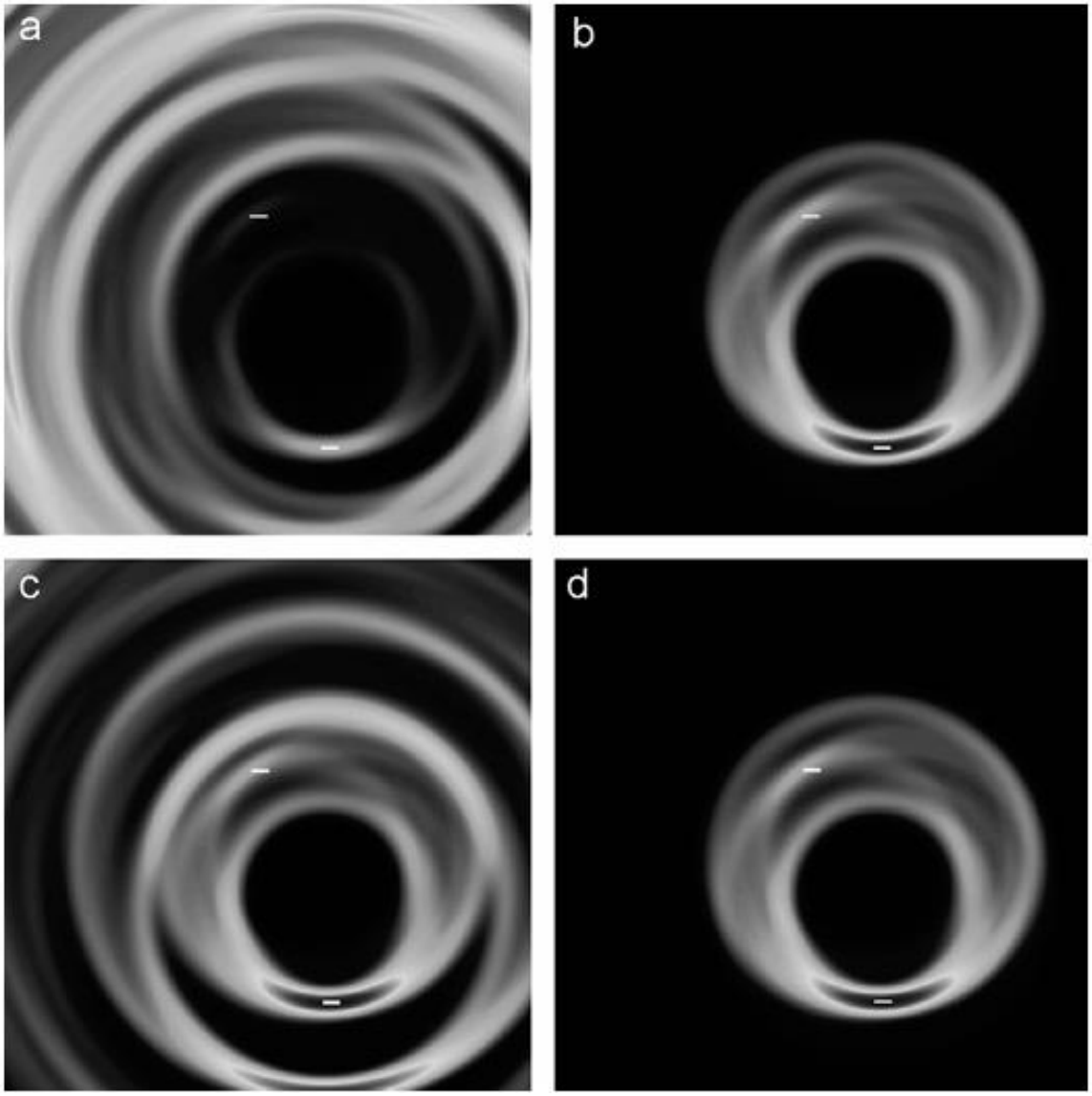

Figure 1.19 Damage influence map of numerical results [30].

The spectral element method in this study is successful in damage detection and creates a monitoring system using the clock-like array that is more effective than the traditional dispersive sensor array [30]. However, this system requires complex analysis to determine the

damage detection algorithm and it requires a highly trained technician to interpret the signal characteristics.

1.4 Challenges and Motivation for Embedded Ultrasonic Inspection of Liquid Filled Pressure Vessels

The existing techniques established face challenges in their complexity and interpretation of the signal characteristics. These issues arise as a result of the complex propagation modes of the signal through the structure and their sensitivity to a multitude of stimuli including environmental pressure and temperature as well as the material properties of the structure itself. The techniques and methods used require a highly trained technician to conduct the signal analysis and this process is time-consuming. However, the analysis method used in embedded ultrasonic inspection of a liquid filled pressure attempt to combat this using PZTs that are permanently adhered to the test structure. This creates consistent coupling of the sensor to the structure and opens the door for future work to automate this inspection. However, there are still challenges faced in automating this inspection with understanding the changing environment conditions and how the pressure and temperature changes affect signal propagation through the pressurized vessel.

Chapter 2 Theoretical Background

Elastic waves propagate through a material causing deformation in the material under stress. A specific type of elastic wave is a Lamb wave, named after Professor Horace Lamb, who characterized the motion of waves in elastic plates [31]. These waves bridge the space from body waves to Raleigh waves and travel in thin plates through the material with multiple,

complex propagation modes. Two of these propagation modes are well modeled and used in ultrasonic inspection. First is the symmetric mode which operates in tension and compression where the propagation occurs parallel to the surface of the material as shown in **Figure 2.1**.

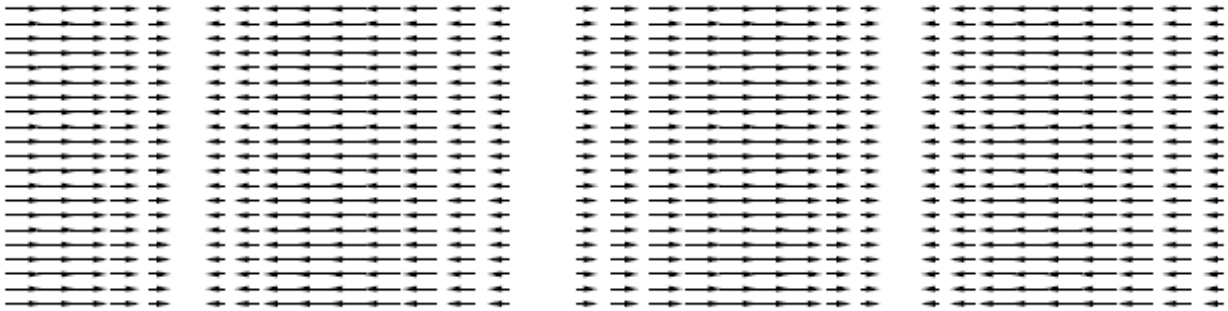

Figure 2.1 Symmetric propagation mode [32].

The next is the antisymmetric mode which operates in bending or flexurally as shown in **Figure 2.2** where the propagation path is more complex compared to the symmetric mode.

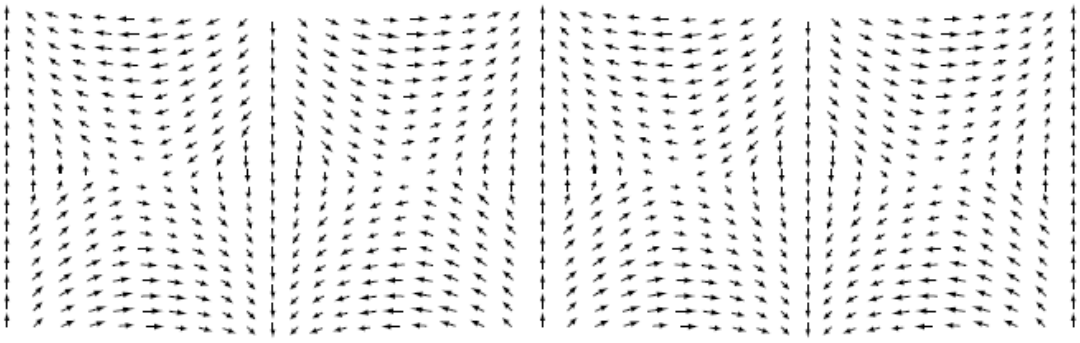

Figure 2.2 Antisymmetric propagation mode [32].

Characterizing the elastic wave propagation into these modes allows ultrasonic inspection methods to understand a signal and interpret the changes in each mode. In signal analysis the symmetric mode is expected to travel quickly through the structure and the antisymmetric mode is expected to be highly sensitive to changes in the surface conditions of a material [32]. Also, the speed of propagation is heavily influenced by changes in frequency of the signal. The

propagation modes are affected differently and there is a different change in the speed of propagation as the frequency changes. This is seen in the dispersion curves of Lamb waves in an aluminum plate are below in **Figures 2.3** and **2.4** with the frequency-thickness (f-d) vs phase and group velocity. The dispersive nature of the waves offers another strategy for signal interpretation and analysis through experimentation [33].

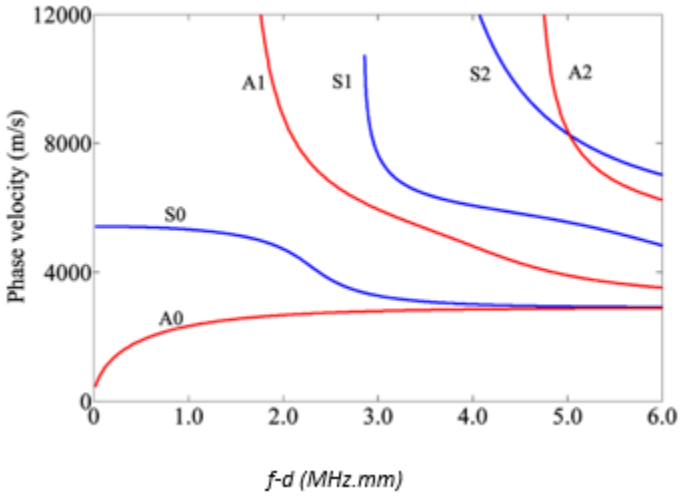

Figure 2.3 Dispersion curve of Lamb waves (phase velocity) [33].

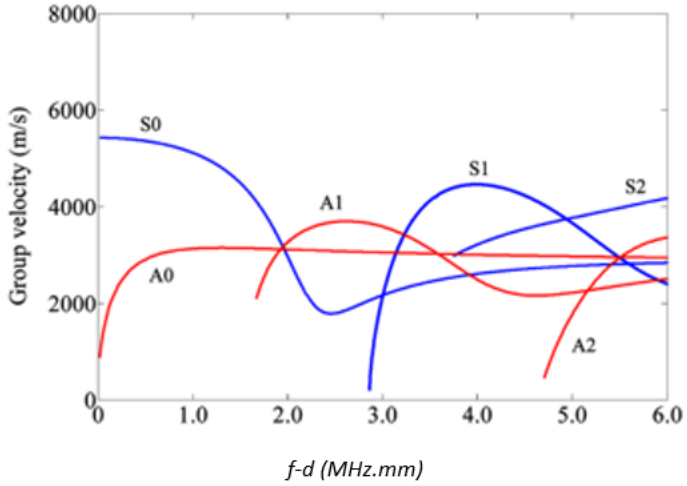

Figure 2.4 Dispersion curves of Lamb waves (group velocity) [33].

In **Figures 2.3** and **2.4**, f-d is measured using a product of the frequency of the signal measured in megahertz (MHz) and thickness of the medium in which the signal is propagated measured in millimeters (mm). Phase velocity is the speed of the particular wave mode as it propagates through the medium and represents the speed at which the phase of the wave travels. Group velocity is the speed of the overall shape of the wave which is a superposition of different wave components as it travels through the medium. Phase and group velocities are both measured in meters per second (m/s) here. The fundamental, first order, and second order both the symmetric and antisymmetric modes are shown in these figures as S0, S1, S2 and A0, A1, A2, respectively.

The method used to propagate the elastic wave through the structure is the embedded pitch-catch method. This method uses embedded sensors on the surface of the structure to actuate and sense lamb wave propagation in the structure. **Figure 2.5** shows an example of this method where there is an actuator that excites waves in the structure and a sensor placed a distance away detects the waves as they propagate.

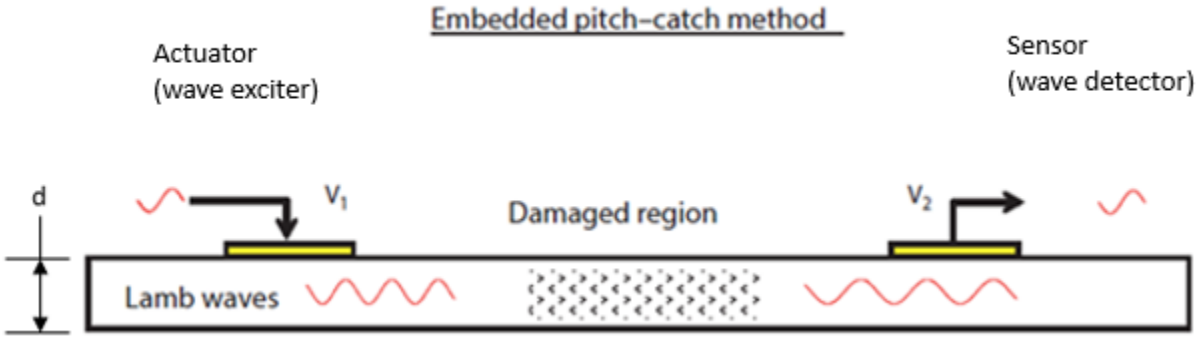

Figure 2.5 Embedded pitch-catch method [32].

In **Figure 2.5**, V_1 is the input voltage of the actuator, V_2 is the output voltage of the sensor, and "d" is the thickness of the medium through which the signal is actuated.

Damage or degradation in the structure will change the wave propagation from the transmitter to the receiver. From here, ultrasonic inspection techniques look to analyze and characterize these changes using the knowledge of different propagation modes. This technique has been established using flat plate with multiple damage metrics including root mean squared deviation (RMSD) as shown in **Figure 2.6**, mean average percentage deviation (MAPD) as shown in **Figure 2.7**, and Cov as previously defined in **Figure 1.8** to characterize how the damage effects the plate [32].

$$\mathrm{RMSD} = \sqrt{\frac{\sum_{i=1}^{N} (x_i - \hat{x}_i)^2}{N}}$$

Figure 2.6 RMSD definition [34].

$$\frac{1}{n}\sum_{i=1}^{n} \frac{|y_i - \hat{y}_i|}{|y_i|} * 100$$

Figure 2.7 MAPD definition [35].

In **Figure 2.6**, N is the number of measurements, x_i is the pristine waveform signal and $\hat{x}_i$ is the measured signal output from the system. In **Figure 2.7**, n is the number of measurements, y_i is the pristine waveform signal and $\hat{y}_i$ is the measured signal output from the system. As mentioned, these damage metrics will be used in signal analysis as the and investigation will

occur based on the differences in pristine and measured signal to quantify damage. Expert knowledge of the system is required to use the damage metric to relate this to differences in the multiple waveform propagation modes phase and group velocities of the propagating signal.

Furthermore, with a complex structure this can be extremely challenging with environmental affects and multiple propagation modes occurring simultaneously, so the experimental approach is paired with the theory of wave propagation to make conclusions about the changes and appropriate damage metric selected.

Chapter 3 Experimental Approach

Ultrasonic inspection uses the theoretical background as a starting point, but it is highly dependent on the experimental data as there are a number of factors that can change how a signal propagates through a structure. The experimental approach looks to explore the fundamental capabilities of embedded ultrasonic inspection on the tank. Then, use previously established techniques for basic structures and apply them to a complex pressurized water tank structure. After there is an understanding of the elastic wave signal propagation in the water tank, further investigation into how changing tank conditions from simulating damage, empty/full tank, and pressurizing the tank will affect the signal propagation.

3.1 Testbed Creation

The complex pressure vessel used for the experiment is a 6-liter on-demand water heater tank with curved geometry and weld lines that will affect signal propagation [36]. Five PZT sensors were mounted to the outside of this tank on the outer surface with the tank itself serving as the

electrical ground. The locations for the sensor placement were chosen to spread across the tank geometry. Sensors were placed on all sides of the tank strategically so analysis could be done on how different distances from the actuating signal and tank geometry and weld lines affect wave propagation. PZT locations are shown below in **Figures 3.1-3.3**. In these figures, the actuator, sensor #1, sensor #2, sensor #3, and sensor #5 positions are defined. There is no sensor shown as sensor #4 as the sensor placed and labeled sensor #4 did not have a strong adhesion to the surface and was removed later in testing.

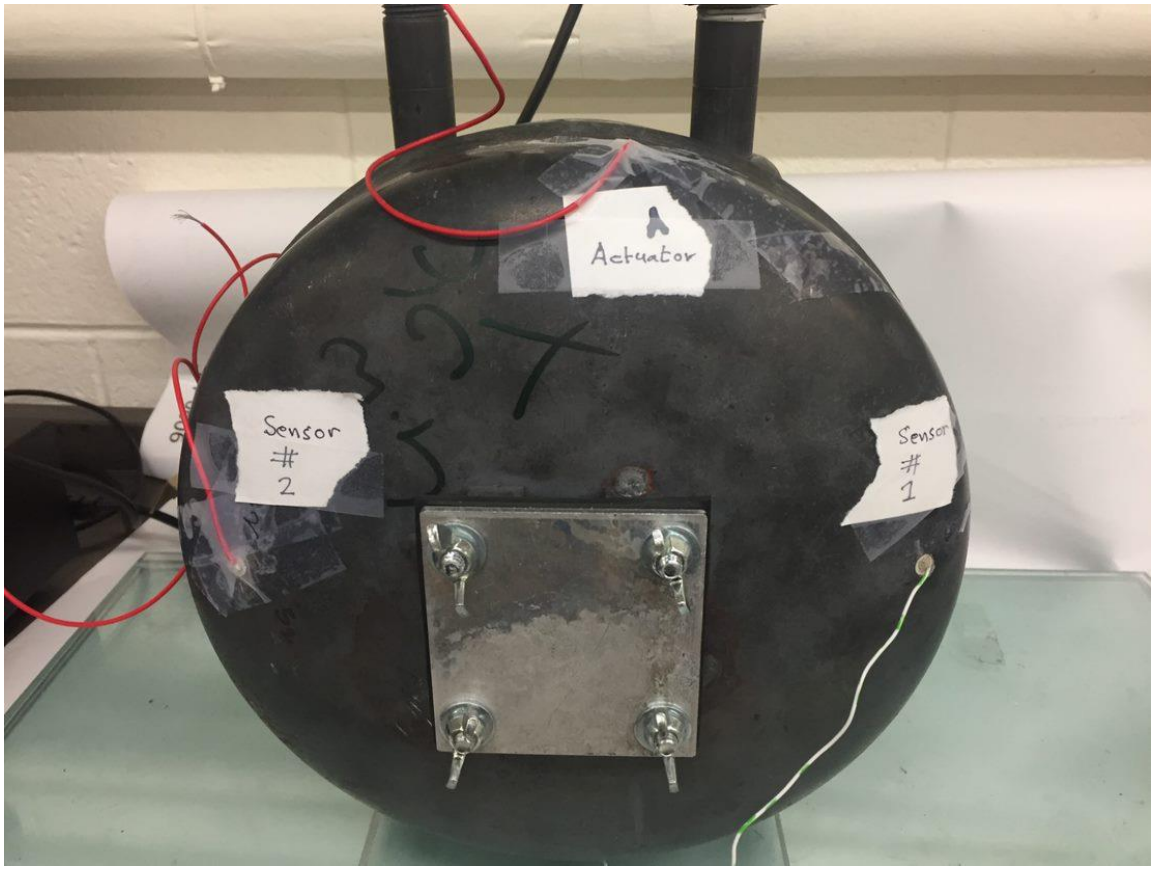

Figure 3.1: Sensor location on the front of the tank, actuation sensor on top of the tank, sensor #1 and sensor #2 on right and left side of the tank, respectively

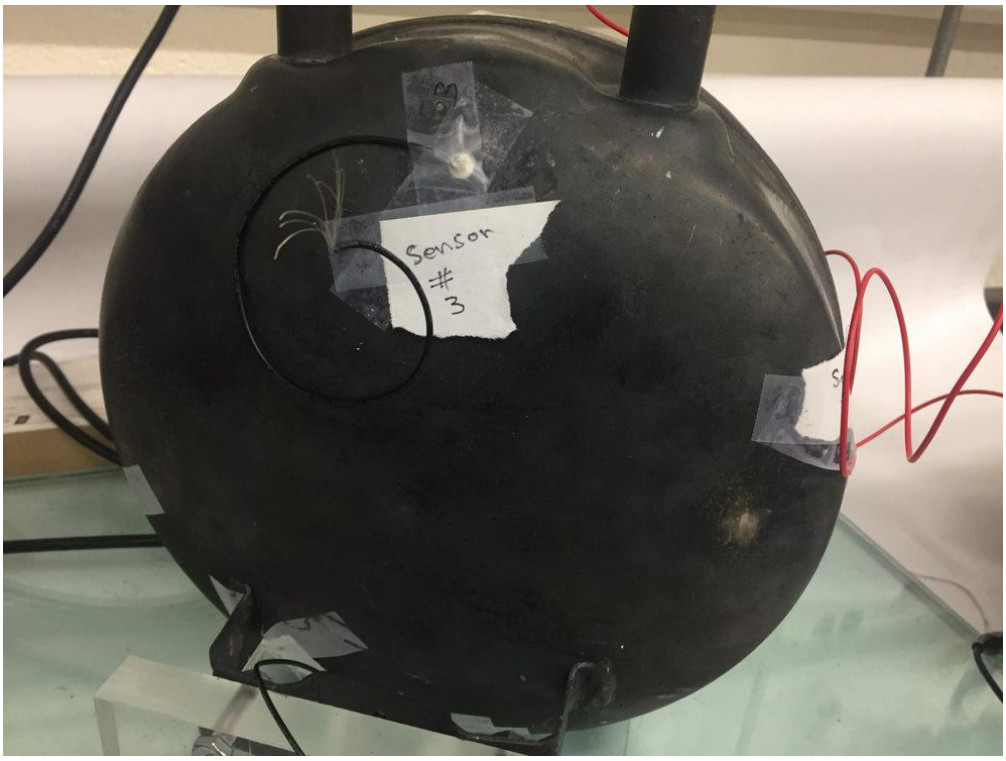

Figure 3.2: Sensor location on back, top of tank labeled on tank as sensor #3

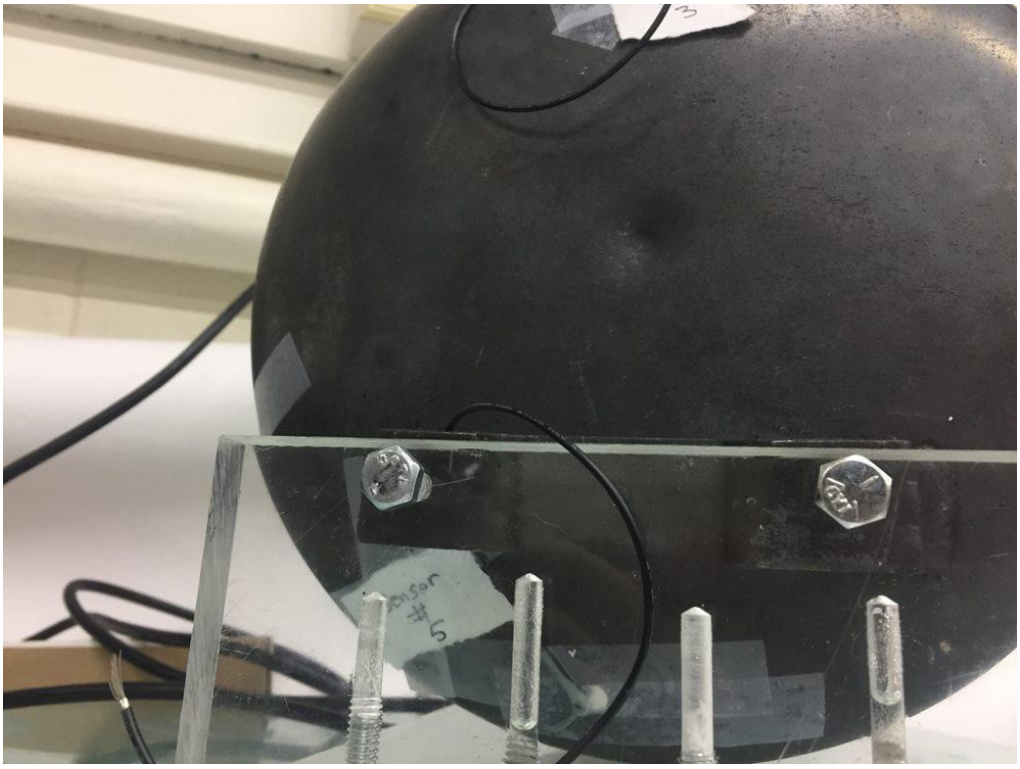

Figure 3.3: Sensor location on back, lower side of tank labeled on tank as sensor #5

To mount them, the surface of the tank was sanded first to remove any paint from the exterior and the PZTs were mounted using a CircuitWorks 2400 conductive epoxy to promote strong signal propagation and minimize outside effects [37] as shown in **Figure 3.4-3.5**. Any of the PZTs can be used as the actuator with the others used for sensing.

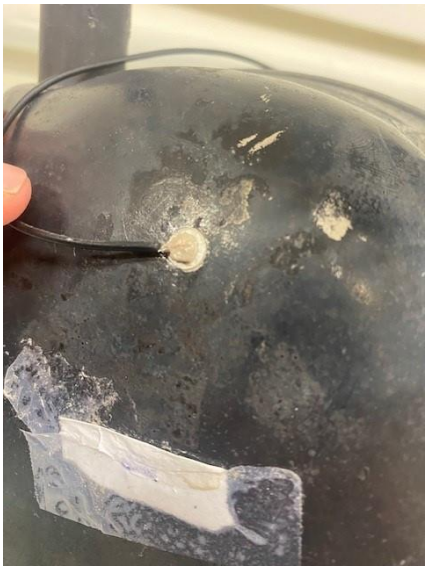

Figure 3.4: Close up view of PZT mounted on tank.

Figure 3.5: Additional close up view of another PZT mounted to tank.

From there, the tank was altered to add components to allow for pressurization of the structure. Attached to one of the tank ports on the top of the structure, where the top is defined by how tank was mounted to supporting structure and displayed in the figures, is a pipe tee with a pressure gauge and a long pipe nipple extending two feet above the tank structure. At the top of this structure is a pipe tee with a Schrader valve and ball valve attached to the top as shown in **Figure 3.6**.

Figure 3.6: Schrader and ball valves connected to the top of the tank structure.

The pipe extension allows for a head of water far above the top of the tank, so the tank remains completely full of water as it is pressurized. The tank is pressurized with air using the Schrader valve at the top of the pipe extension with the ball valve as the manual pressure relief valve. Attached to the other tank port is a larger ball valve to allow for ease of use in filling or emptying the tank. The full structure is shown below in **Figure 3.7**.

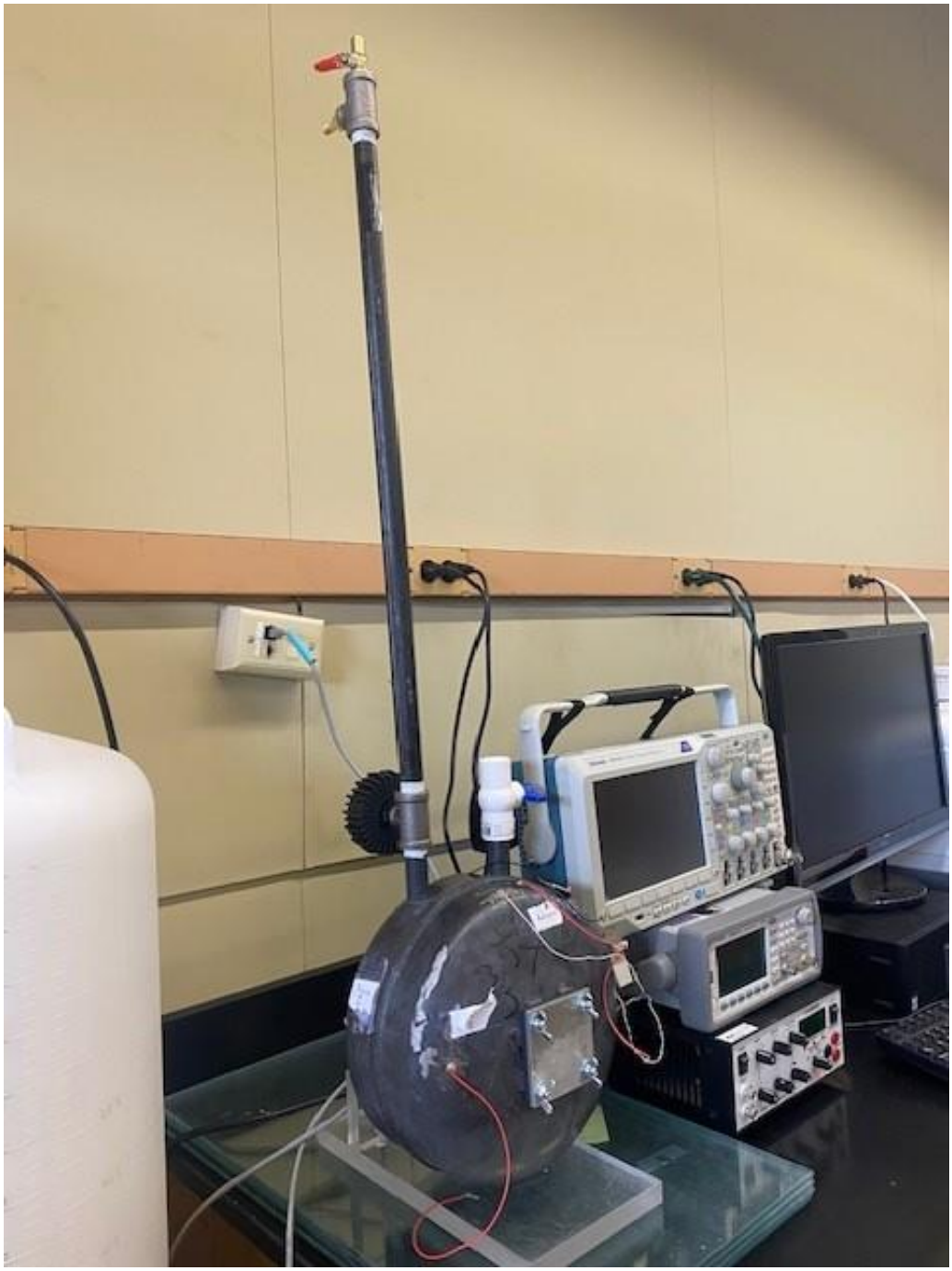

Figure 3.7: Full tank structure used in testing.

3.2 Methods

The experimental setup begins with the waveform generator which creates a time-modulated actuation voltage signal. The waveform generator can produce a range of input signals, but the one selected for the ultrasonic experiments is a five-cycle Hanning-windowed tone burst. This signal was chosen as it is limited in both time and frequency domains. Being limited in those domains helps the wave packet to stay intact as it propagates through the structure as signal velocity is dependent on the frequency [38]. **Figure 3.8** below shows an example of a Hanning-windowed tone burst signal and its frequency spectrum.

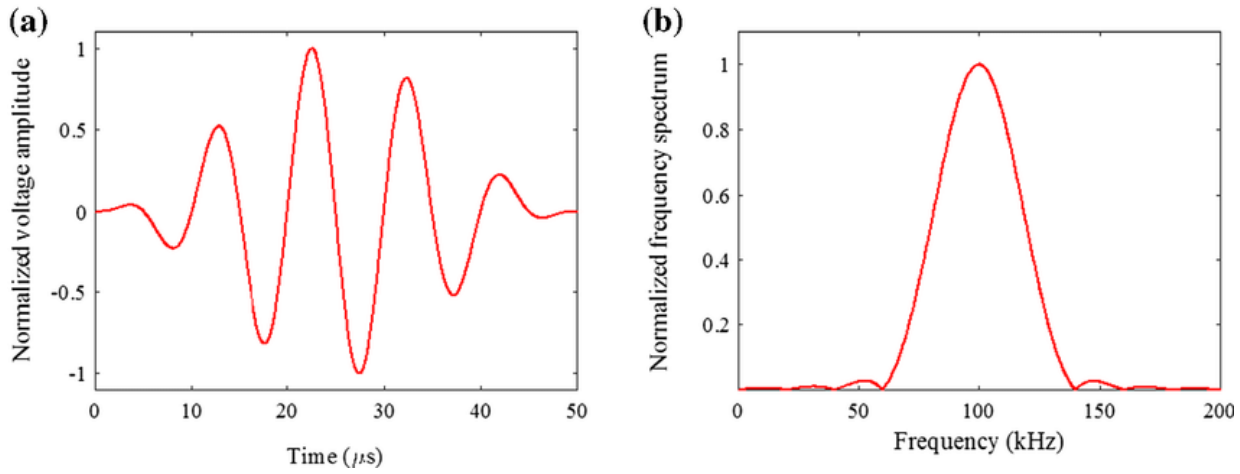

Figure 3.8: (a) Five-cycle Hanning-windowed tone burst input signal with a center frequency of 100 kHz (b) its frequency spectrum presented [38].

The actuation signal is then amplified using the voltage amplifier to increase the signal to noise ratio. Without the amplification of the signal, it is difficult to differentiate if small changes are attributable to changes in the sensing signal or to random noises. Once the signal passes through the amplifier, it is applied to the selected PZT on the tank structure. As mentioned, the PZT used as the actuator is shown on the top of the tank in **Figure 3.1** for all the experimental results shown in Chapter 4. Then, an oscilloscope is used to record the actuation signal and

response of the other PZTs on the structure. Finally, the signals are transferred from the oscilloscope to a computer to analyze different signal characteristics of the response. Below in **Figure 3.9** is an overview of the process and systems used for the experiment.

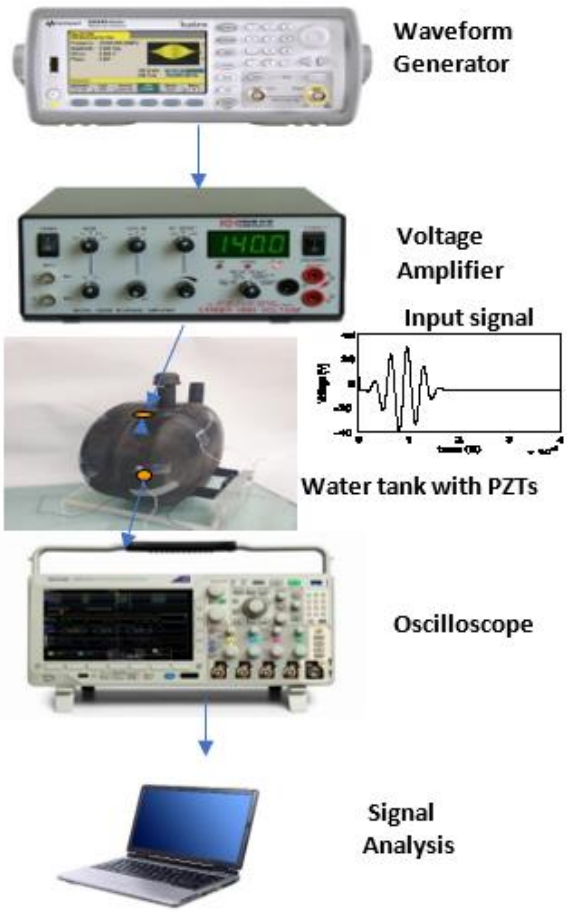

Figure 3.9: Ultrasonic SHM experimental setup.

3.3 Resonance and Peak Frequencies

Initial testing was conducted on the tank structure to determine the natural and peak frequencies of the tank structure. Three methods were used to do this including the manual method, Welch method, and chirp method. The manual method uses an input sine wave signal

that was manually varied while the oscilloscope was observed watching for peak amplitude outputs, sweeping across the desired frequency range and the sensor response output voltage is recorded [39, 40, 41]. **Figure 3.10** below shows the results using the manual method with the signal sweeping from 100 to 500 kHz.

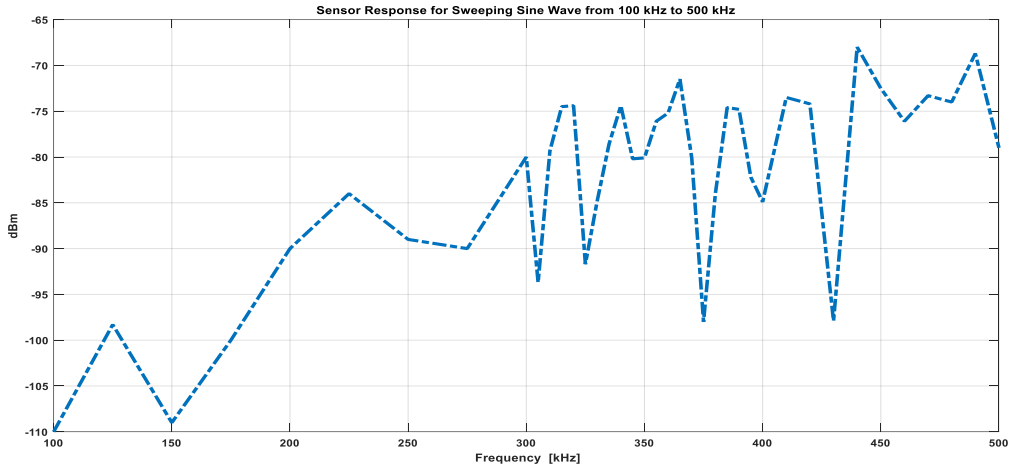

Figure 3.10: Manual method sensor response for sweeping sine wave.

The Welch method uses an input random noise signal with a bandwidth spanning the frequency range [42, 43, 44]. The highest voltage output response of three sensor responses are shown below in **Figure 3.11**. The frequency range used for this method was from 100 to 500 kHz with the plots showing the range of 300 to 450 kHz where each of the peak values were found.

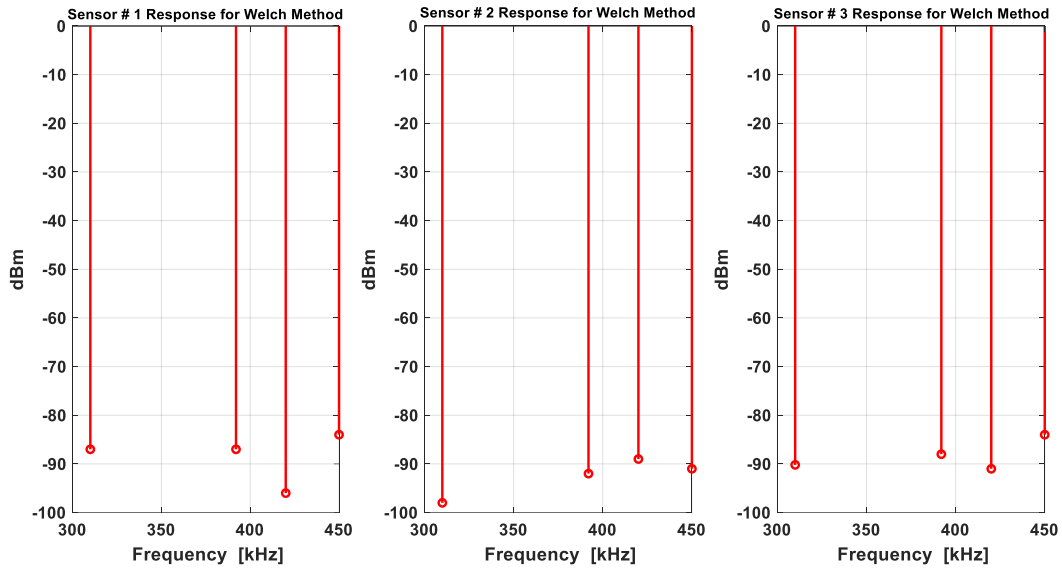

Figure 3.11: Welch method sensor responses

Lastly, the chirp method uses an input signal spanning a range of frequencies similar to the manual method. However, in this method Fourier's transform is applied to the output signal and the highest voltage outputs are measures [45, 46, 47]. The results of the chirp method are recorded below in **Figure 3.12** with the frequency spanning from 100 to 500 kHz.

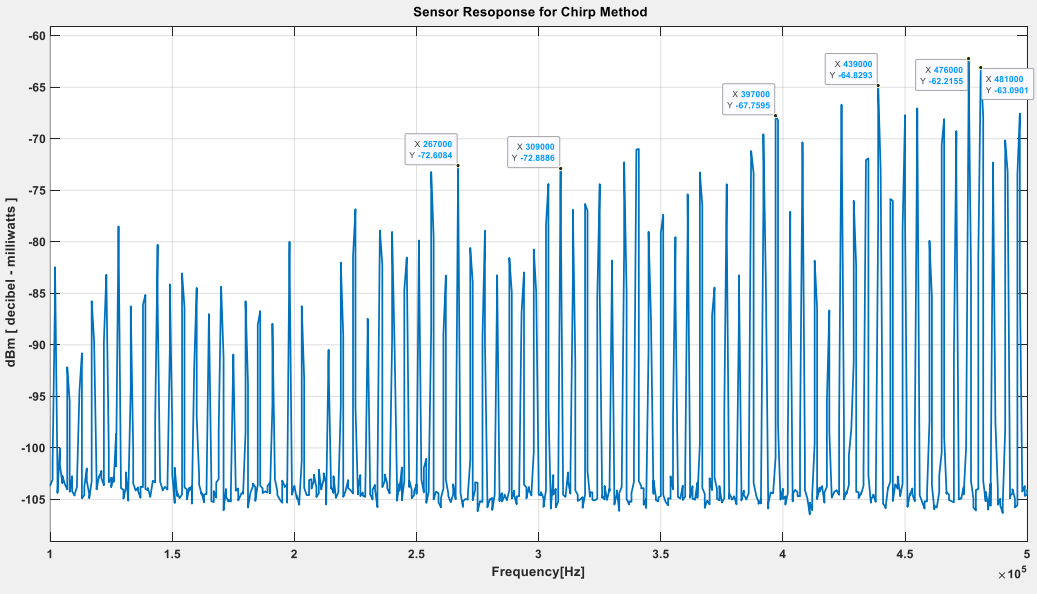

Figure 3.12: Chirp method sensor response

Through testing it is observed in these methods that the resonance frequency of the tank is the same as the natural frequency of the PZTs themselves at 309 kHz. The three methods were used to confirm the results of each other and in all three methods the peaks in the sensor response were seen at 309, 390, 440, and 490 kHz. Frequency tuning of the system is an important step to conduct prior to ultrasonic inspection. Identifying and using the peak frequency outputs of the structure for the actuation signal promotes a strong sensing signal response, further increasing the signal to noise ratio. Further, the identification of the natural frequency can be used in signal analysis as a shift in the natural frequency of the structure can be an indication of degradation in the structure [48, 49].

Chapter 4 Experimental Results and Discussion

The initial tests explore the use of ultrasonic inspection techniques on the tank and using techniques for signal analysis to understand how the signal is propagating. Next is testing with simulated damage where two different size magnets were placed on the test structure between the actuator and sensor to simulate damage in the structure and analyze the signal change. Then, a brief discussion of the concern in the use of the voltage amplifier and its effect. Finally, the last experiment tests the tank structure with varying tank conditions by testing the tank at 10 pounds per square inch (psi). increments from 0-40 psi when the tank is both empty and full of water. All the experiments used the Hanning-windowed tone burst with a center frequency of 300 kHz as the actuation signal applied to the sensor on the top of the tank as shown in **Figure 3.1**. The center frequency of 300 kHz was chosen for the Hanning window based on an estimate of the structure's natural frequency. Future testing will look to refine the system and

experimental process to use the resonance frequency of 309 kHz or other peak frequencies found in the structure testing to promote the strongest signal strength.

4.1 Initial results

Initial experimental results focused on the objective of investigating the fundamental capabilities of embedded ultrasonic inspection using the tank structure. Testing took recordings of the actuation signal and accompanying sensor response of all five sensor locations on the tank shown in **Figure 4.1-4.6** with an empty tank at ambient pressure. From this initial testing, the signal propagation can be analyzed to look at the key characteristics of time of flight for the wave propagation, signal amplitude, and overall signal appearance. Specifically, these signal characteristics in the first wave packet arrival are of interest as analysis past the first or second wave packet gets complex with multiple propagation modes possible and constructive and destructive interference of the signal [50, 51].

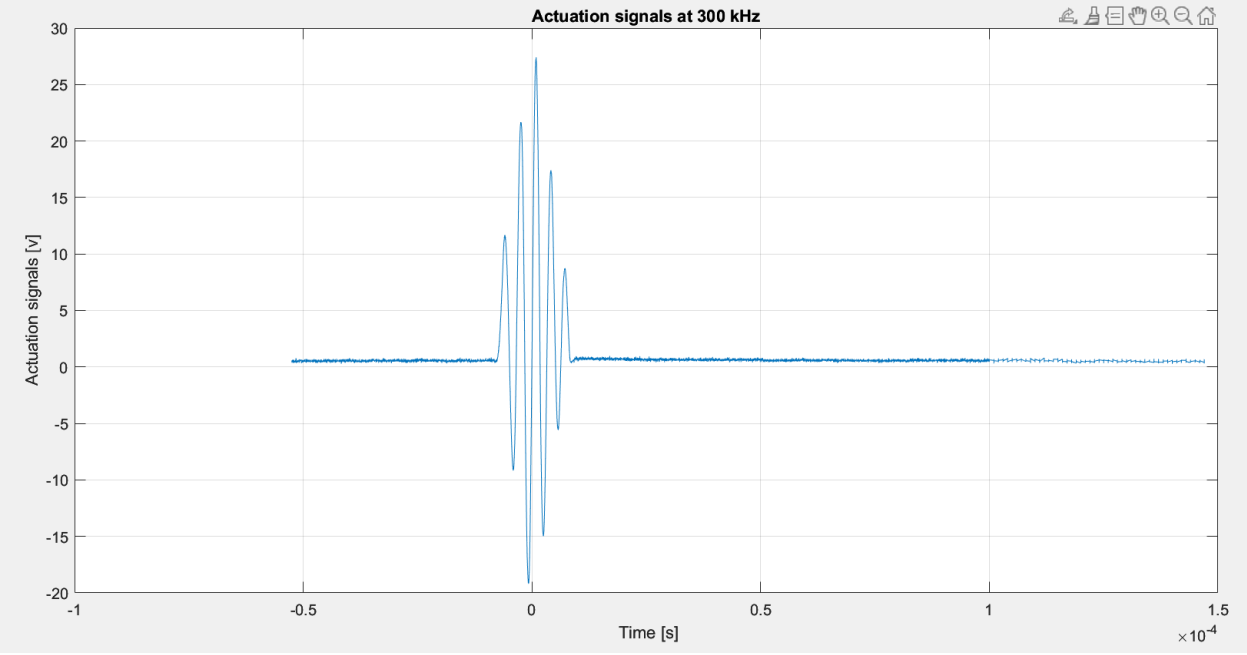

Figure 4.1: Actuation signal from initial test

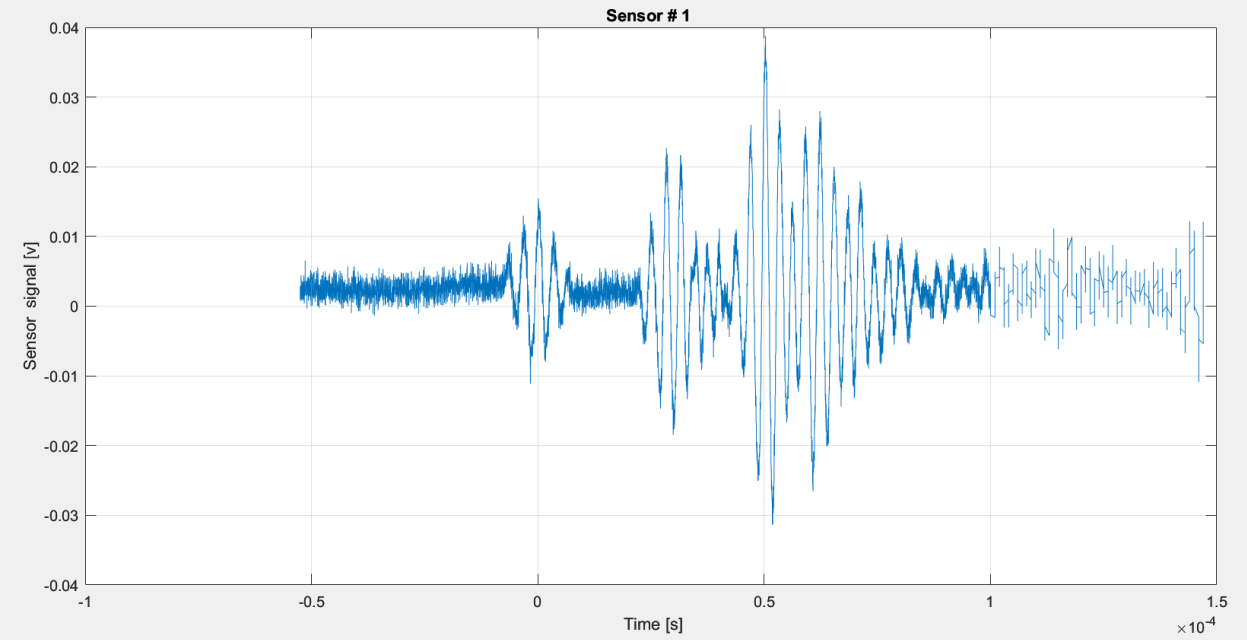

Figure 4.2: Sensor #1 sensor response from initial test

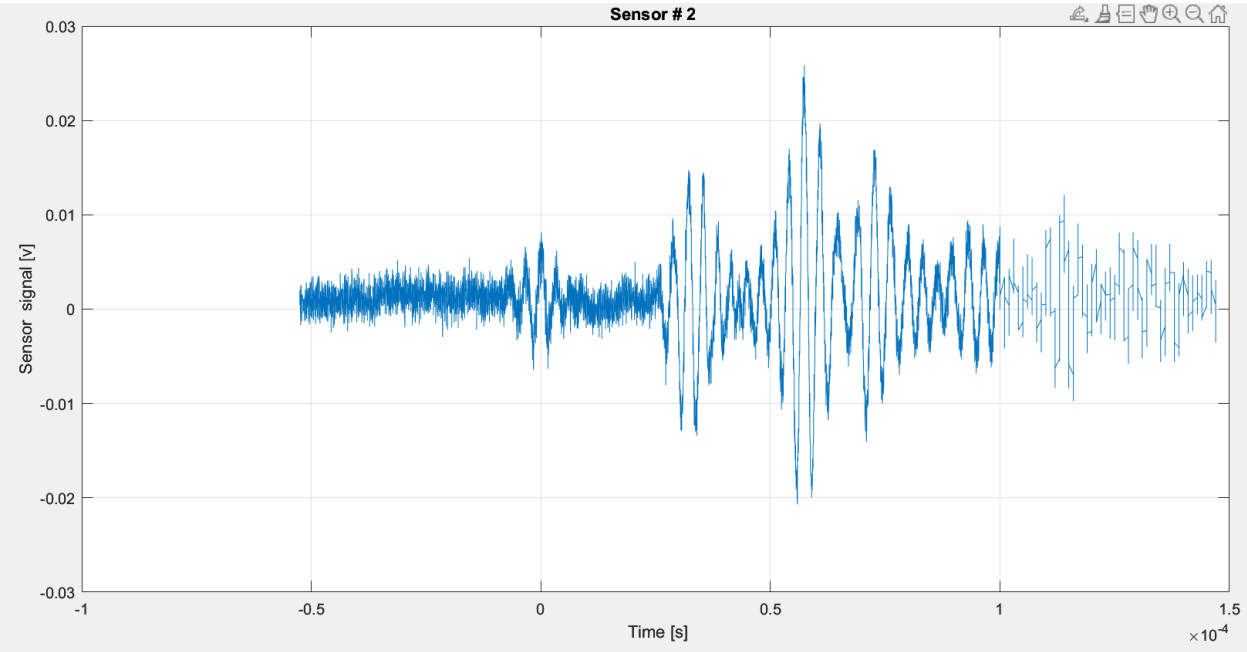

Figure 4.3: Sensor #2 sensor response from initial test

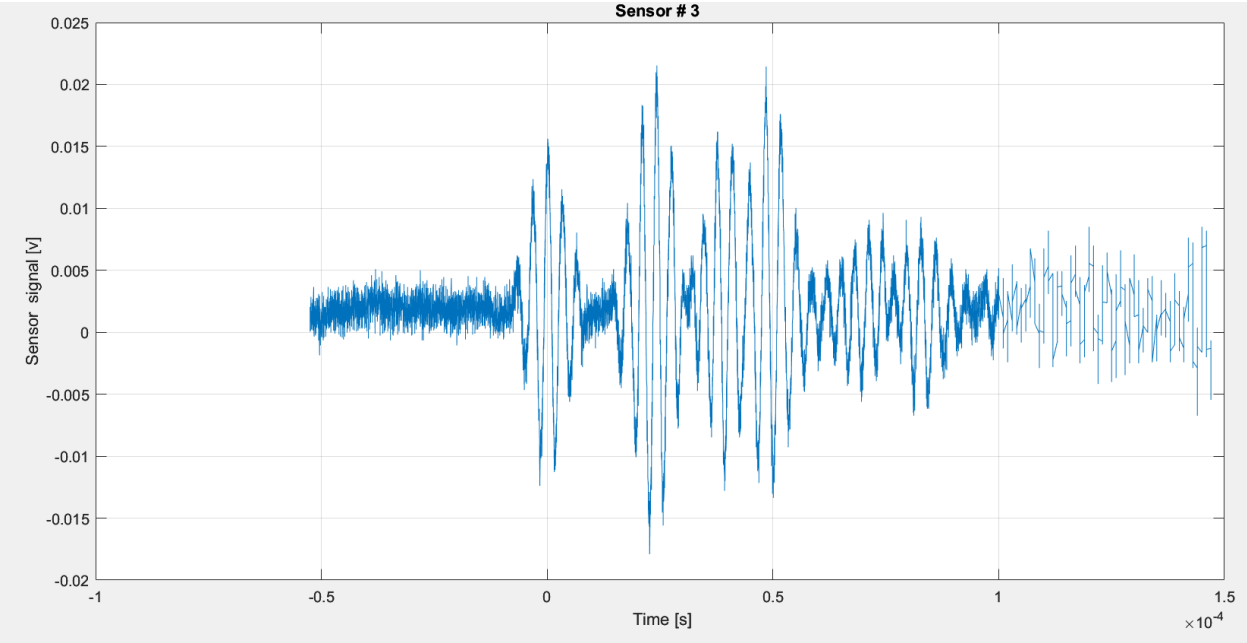

Figure 4.4: Sensor #3 sensor response from initial test

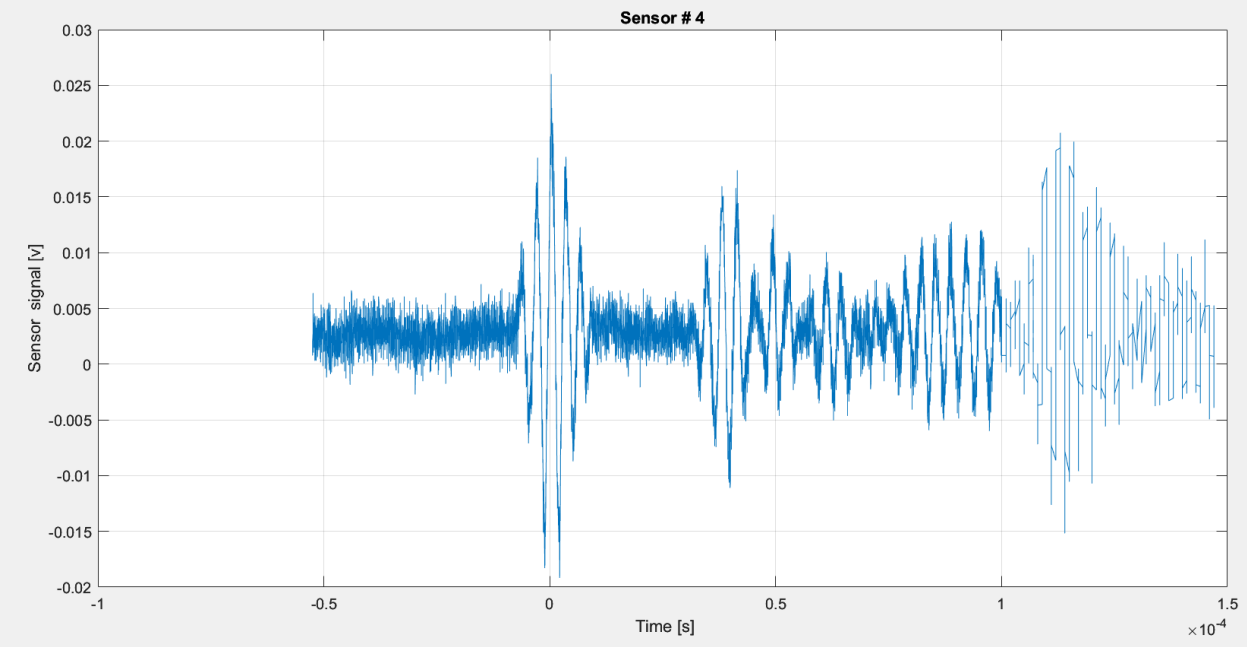

Figure 4.5: Sensor #4 sensor response from initial test

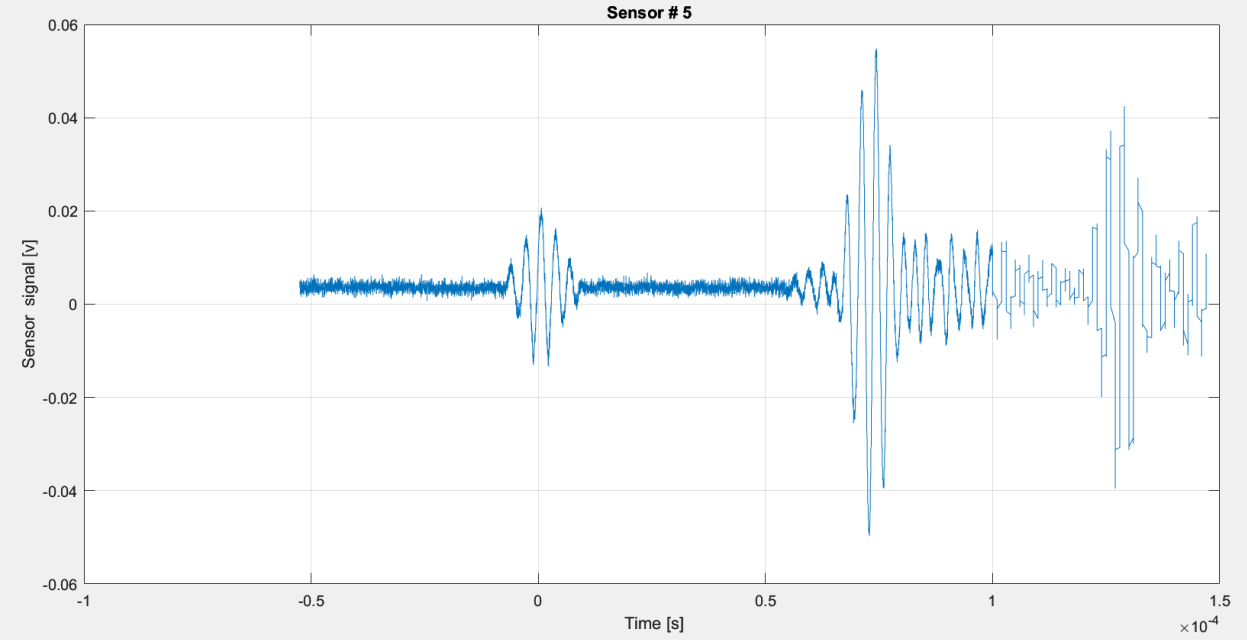

Figure 4.6: Sensor #5 sensor response from initial test

From these results the signal response is strong, and the two main propagation modes can be identified. The first wave packet arrival is the symmetric mode, which propagates faster through the structure than the other propagation modes. Past that, the antisymmetric mode can be seen arriving after the symmetric mode, but the signal begins to get complex as constructive and destructive interference begin to occur and further analysis focuses on the symmetric mode arrival.

The time of flight (ToF) and amplitude of the sensor response is dependent on the position of the sensor with respect to the actuating sensor. When the sensor is very close to the actuator, the sensor response ToF is very short and the amplitude is higher as shown in **Figure 4.2-4.4** with sensor #1, 2, and 3. However, when the sensor position is farther from the actuator, as shown in **Figure 4.5-4.6** with sensor #4 and 5, the first wave packet arrival is later and of lower amplitude. Sensor #5 is on the opposite side of the tank from the actuator and there is

significant constructive interference observed after the first wave packet arrival. This can likely be attributed to the signal propagating in multiple directions through the tank and arriving together near the same time, but the focus is on the arrival of the first wave packet just before this spike.

4.2 Simulated damage on empty tank structure

Damage on the tank is simulated using neodymium magnets. For the experiments, small and large magnets were placed on the tank between the actuator and sensor. Trials were performed with the magnet in three different positions: in a middle distance between the actuator and sensor, near the sensor, and near the actuator. **Figures 4.7** and **4.8** show the magnet positions of the small and large magnets on the tank during testing. The three positions were selected to investigate how ultrasonic inspection of this structure may not only detect the damage to the system, but also locate it. Along with the sensor response for each location, the sensor response with no magnet on the tank is shown together on one graph to comparison each state as shown in **Figures 4.9** and **4.10**.

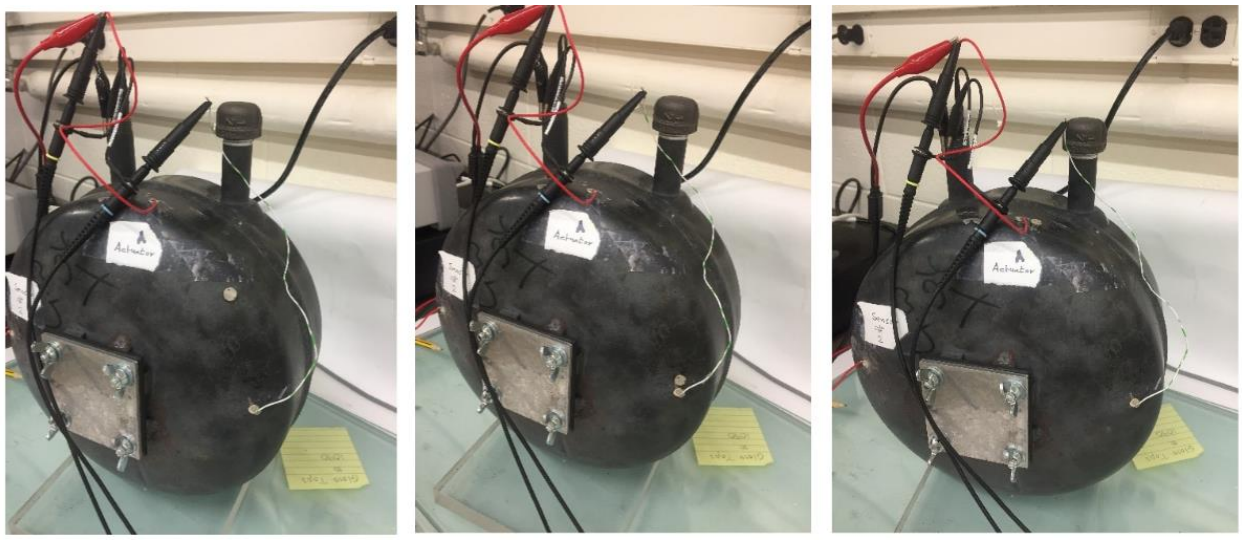

Figure 4.7: Small magnet positions on the structure. From left to right: in a middle distance between the actuator and sensor, near the sensor, and near the actuator.

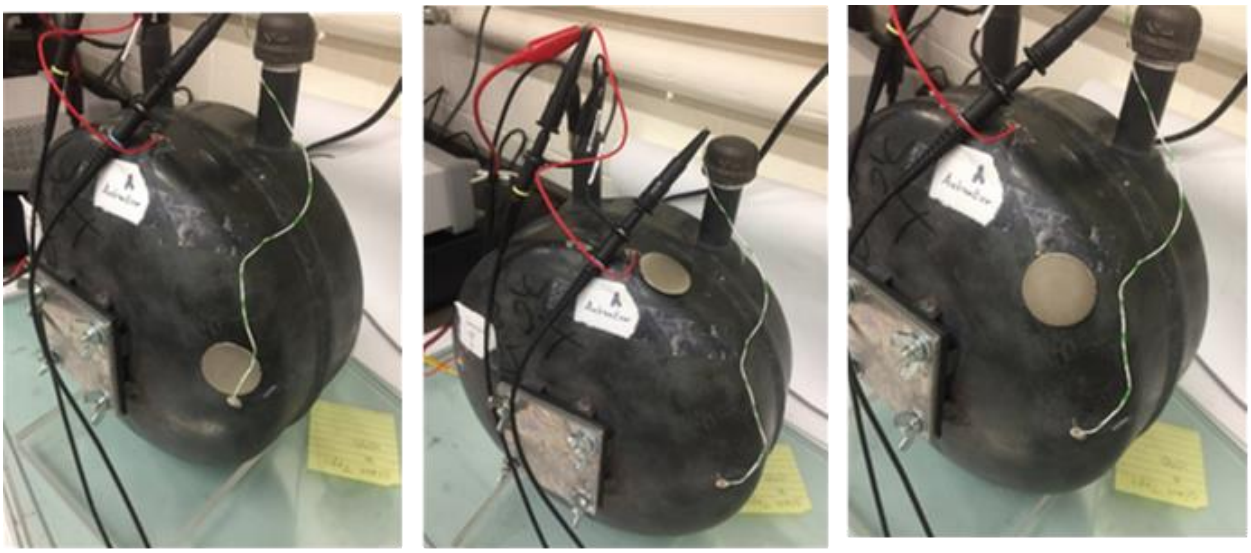

Figure 4.8: Large magnet positions on the structure. From left to right: in a middle distance between the actuator and sensor, near the sensor, and near the actuator.

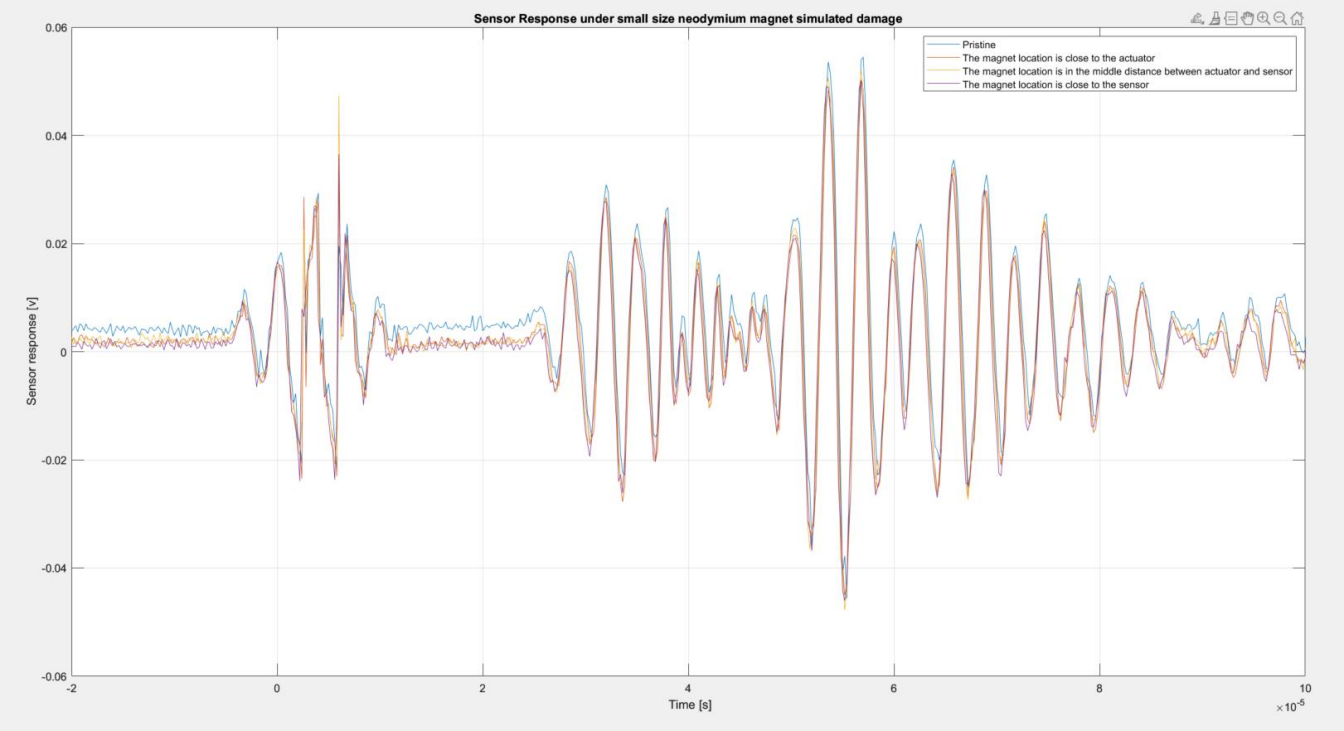

Figure 4.9: Sensor Responses for small magnet simulated damage.

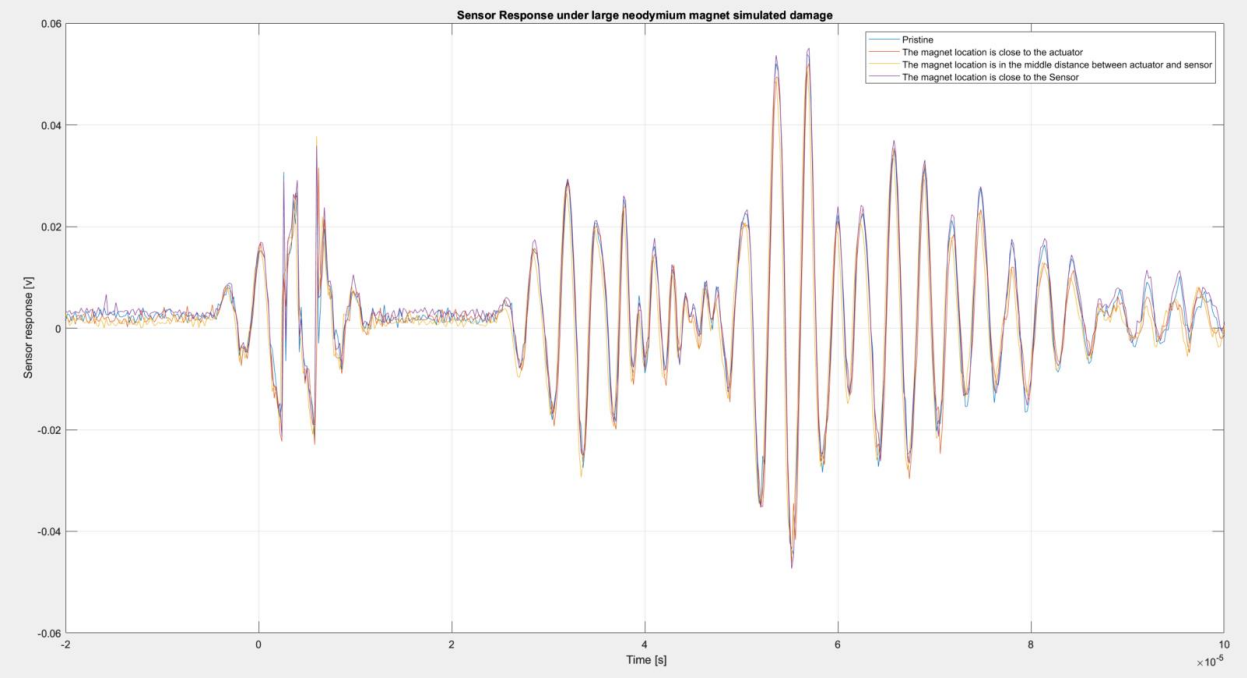

Figure 4.10: Sensor Responses for small magnet simulated damage.

In conducting this experiment, a problem with the voltage amplifier was identified with it distorting the actuation signal and is further explained in the following section. As a result, the small changes in the ToF and amplitude cannot be confidently attributed to the magnet's presence on the structure. However, this experiment shows the capabilities of the system to produce results of this nature when a new voltage amplifier is acquired and implemented. Future work will look to reproduce this testing and characterize the signal changes using one of the damage metrics mentioned in the theoretical background.

4.3 Voltage Amplifier Distortion

The voltage amplifier was identified as the cause for signal distortion by running an experiment with the output of the amplifier connected directly to the oscilloscope. A burst with five cycles of sine wave was used with trials at 100, 200, and 300 kHz for the voltage amplifications of 14, 21, 28, 35, and 42 dB as shown below in **Figures 4.11-4.13** using the waveform generator max voltage output of 8.5Vpp being input to the voltage generator.

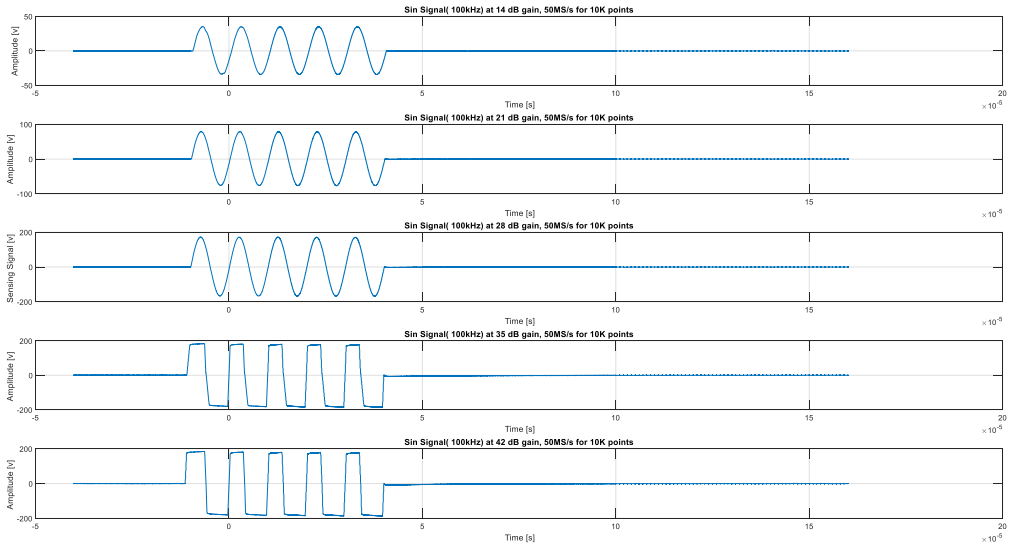

Figure 4.11: Sine wave at 100 kHz at increasing amplification values of 14, 21, 28, 35, 42 dB

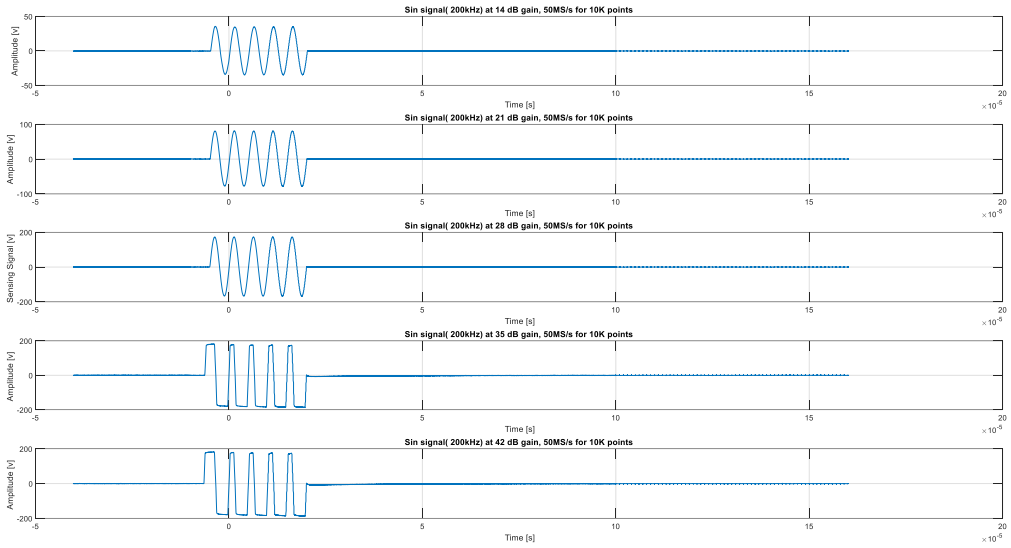

Figure 4.12: Sine wave at 200 kHz at increasing amplification values of 14, 21, 28, 35, 42 dB

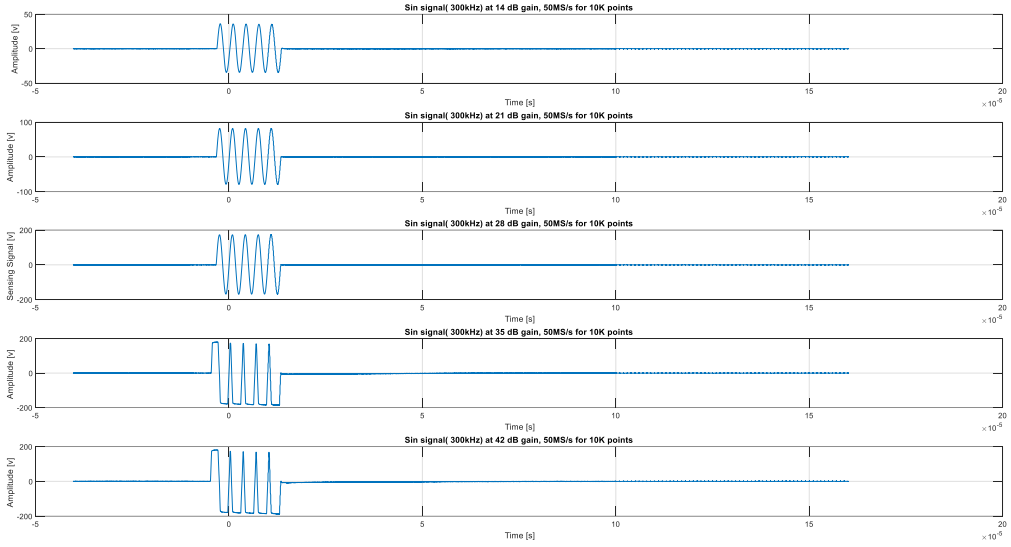

Figure 4.13: Sine wave at 300 kHz at increasing amplification values of 14, 21, 28, 35, 42 dB

It is clear the increase in distortion at the higher amplification levels. To more closely examine the lower amplification levels the sine wave at 300 kHz is plotted with the amplification values of 14, 21, and 28 dB together in **Figure 4.14** and zoomed in on the peaks in **Figures 4.15** and **4.16**.

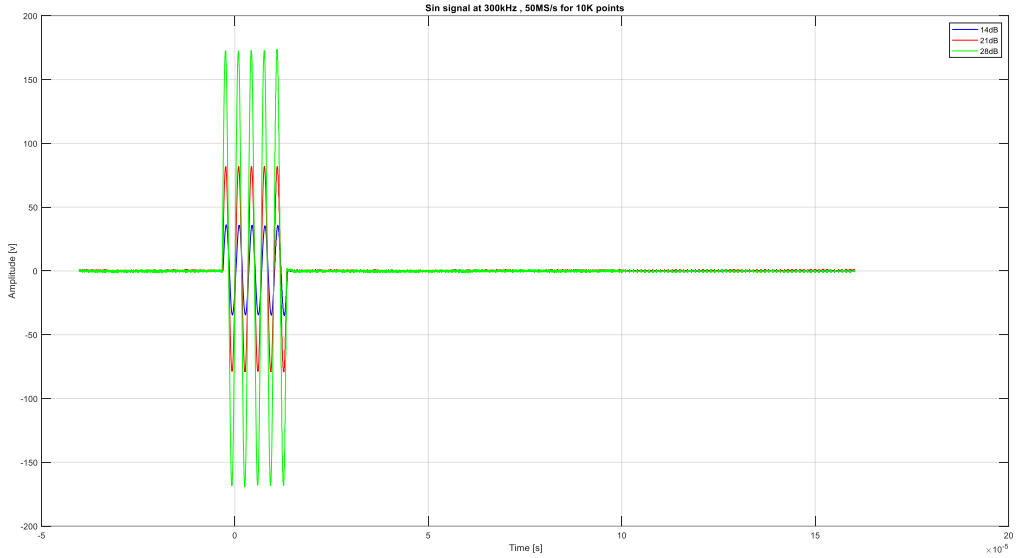

Figure 4.14: Sine wave at 300 kHz with amplifications of 14, 21, and 28 dB plotted together.

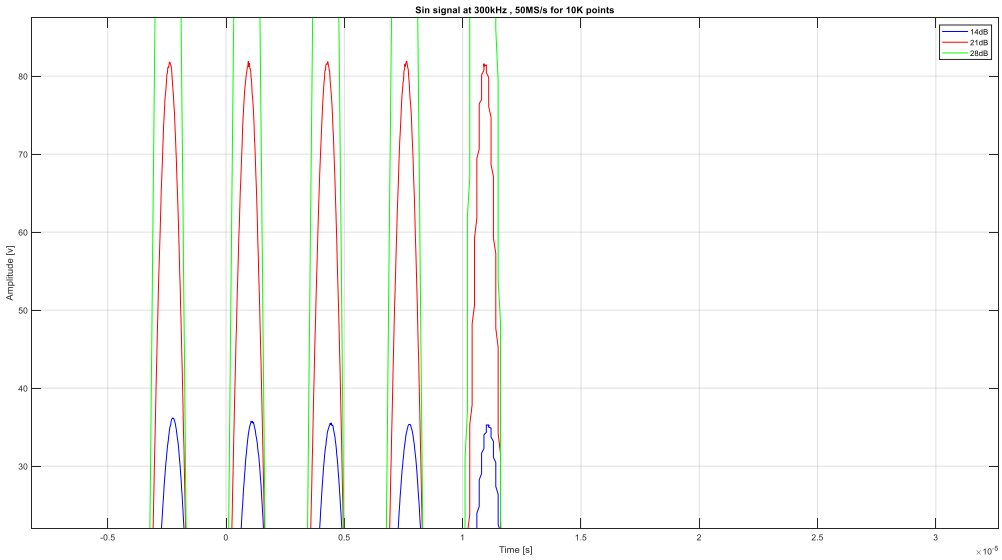

Figure 4.15: Zoomed in snapshot of Figure 4.14 showing the peaks of 14 and 21 dB amplifications.

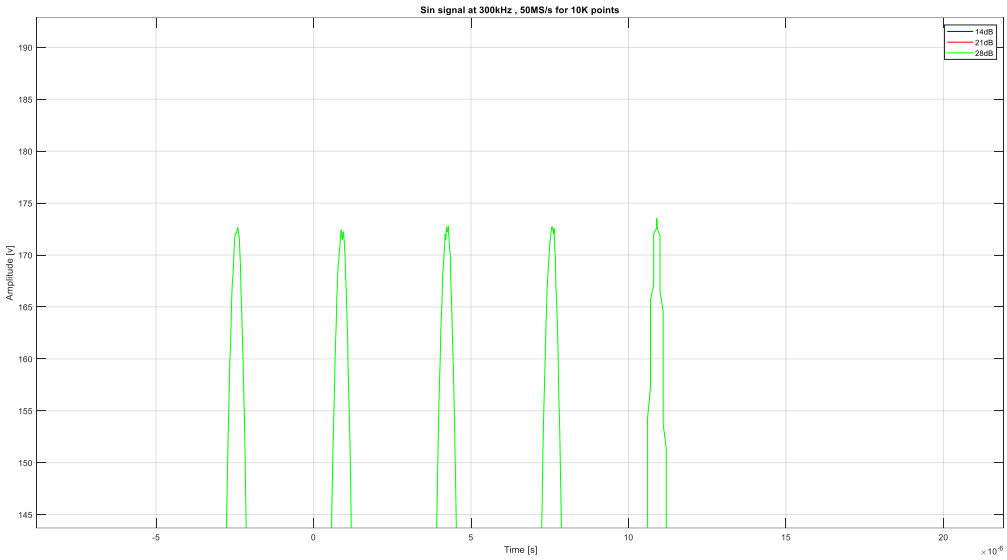

Figure 4.16: Zoomed in snapshot of Figure 4.14 showing the peaks of 28 dB amplification.

The distortion is most clear in **Figure 4.15** and **4.16** at the fifth peak of the sine wave. This distortion will have a clear impact on the sensor response and conclusions about the small changes in sensor response with simulated damage cannot be made.

4.4 Empty and full tank with varying tank pressure

Trials were done first with the tank empty then with it full of water with different pressure conditions. Empty and full tank trials were done at 0 psi, 10 psi, 20 psi, 30 psi, and 40 psi (gauge pressure) to compare for empty and full as well as varying pressure conditions with each trial shown individually the **Appendix**. The actuation signal used is a 300kHz five-cycle Hanning-windowed tone burst applied to the same PZT location on top of tank structure as done previously with the sensor responses of sensor #1, 2, and 3 recorded. However, now the input signal amplitude is 8.5Vpp using the max value of the waveform generator with no voltage amplifier connected to avoid concern in signal distortion.

Next, the plots were combined to analyze the change in sensor response for the empty and full tank at each pressure interval, as shown in **Figures 4.17-4.21**, and for the change in pressure for both the empty and full tank as shown in **Figures 4.22** and **4.23**.

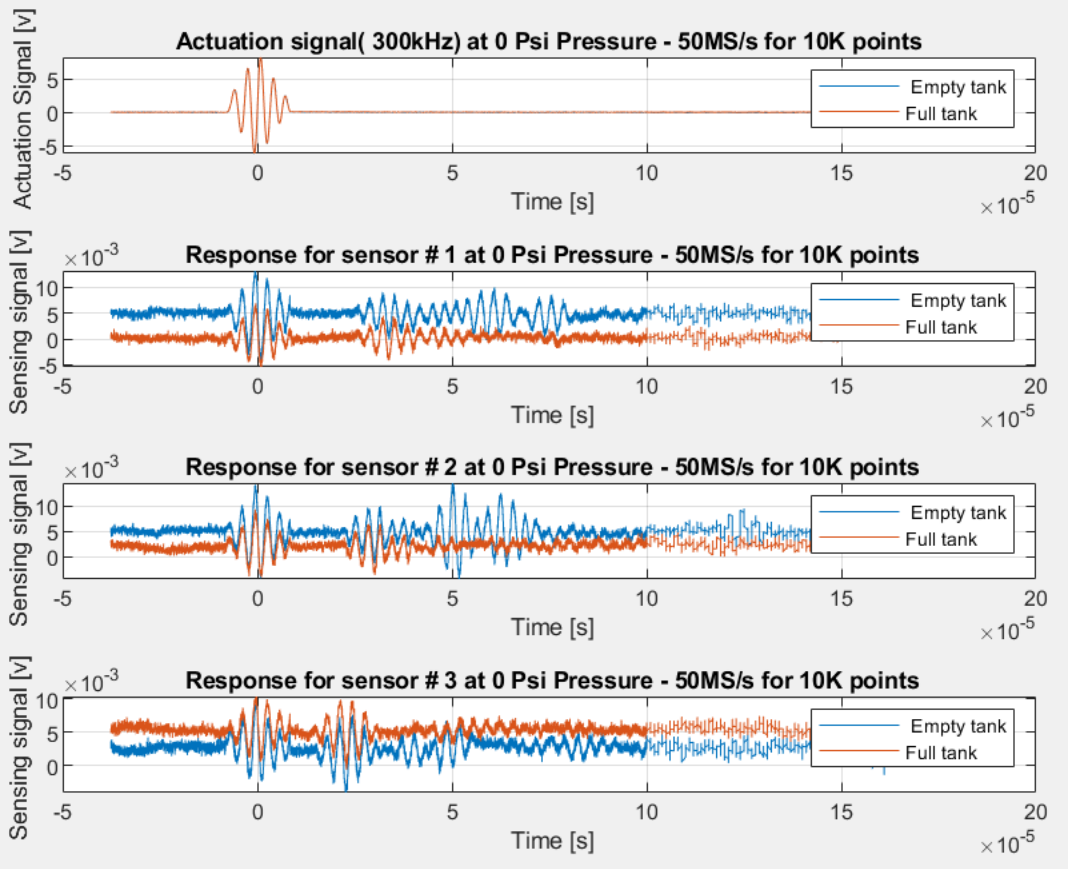

Figure 4.17 Comparison in sensor responses with empty and full tank at 0 psi.

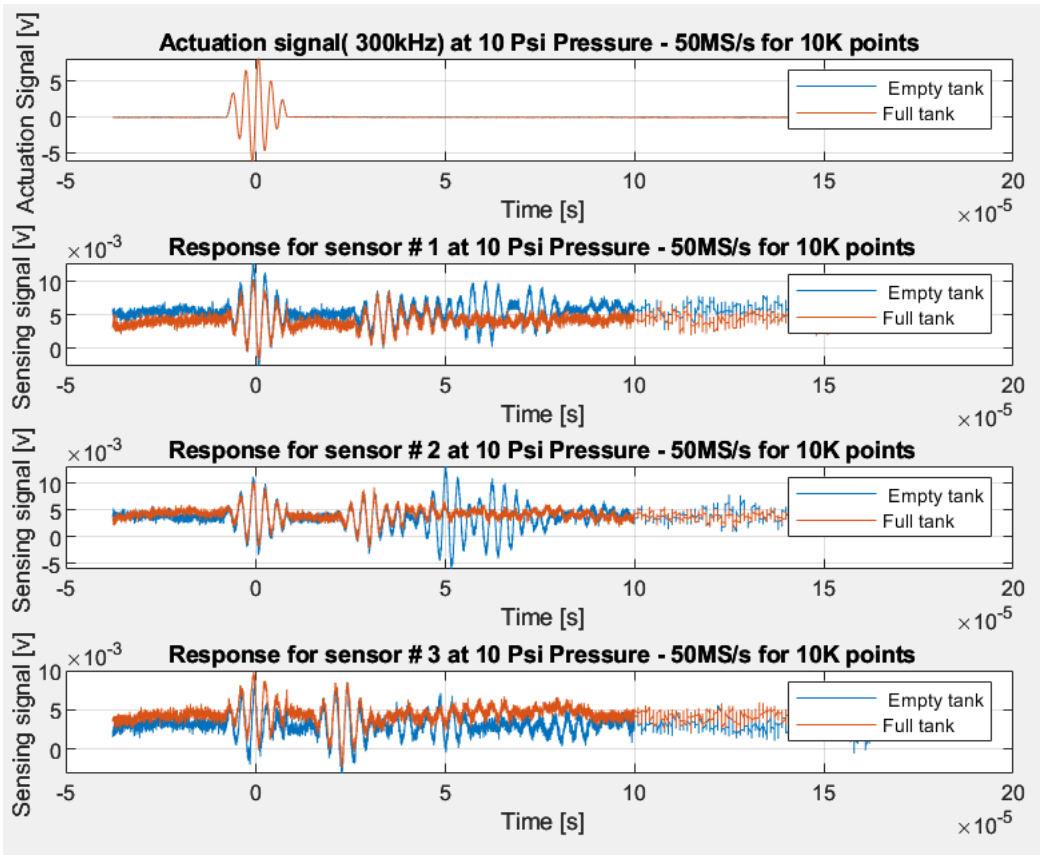

Figure 4.18: Comparison in sensor responses with empty and full tank at 10 psi.

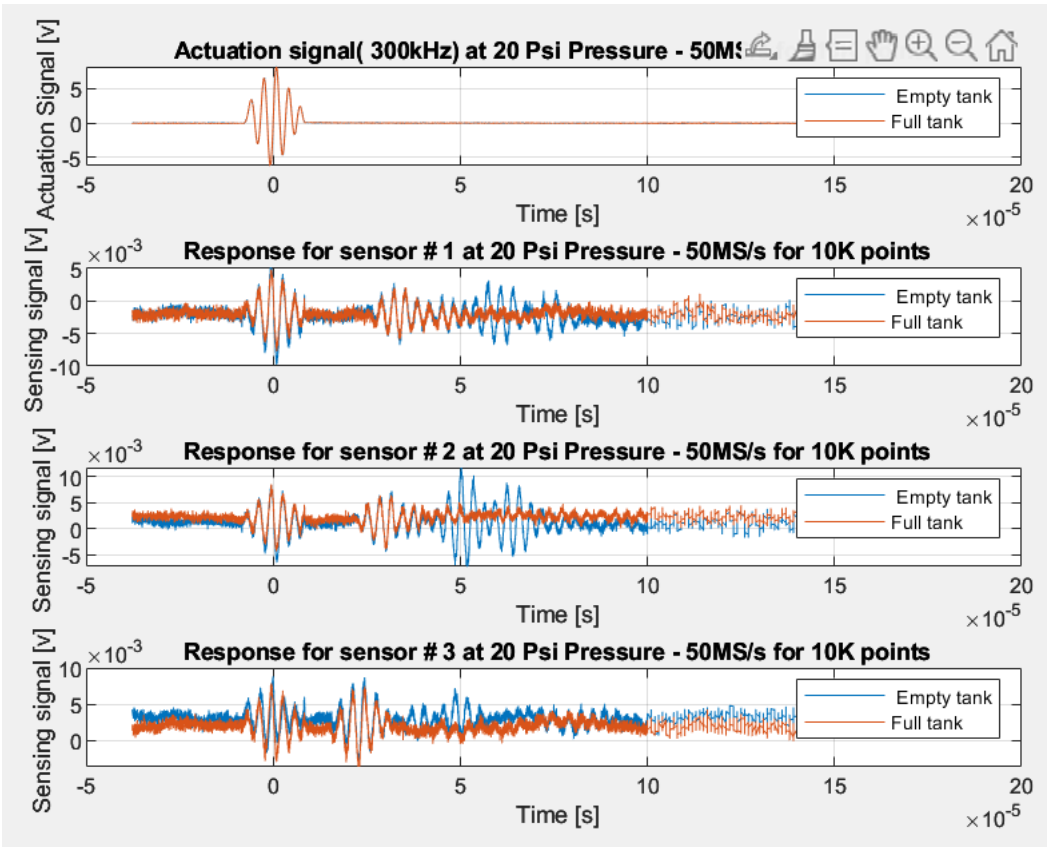

Figure 4.19: Comparison in sensor responses with empty and full tank at 20 psi.

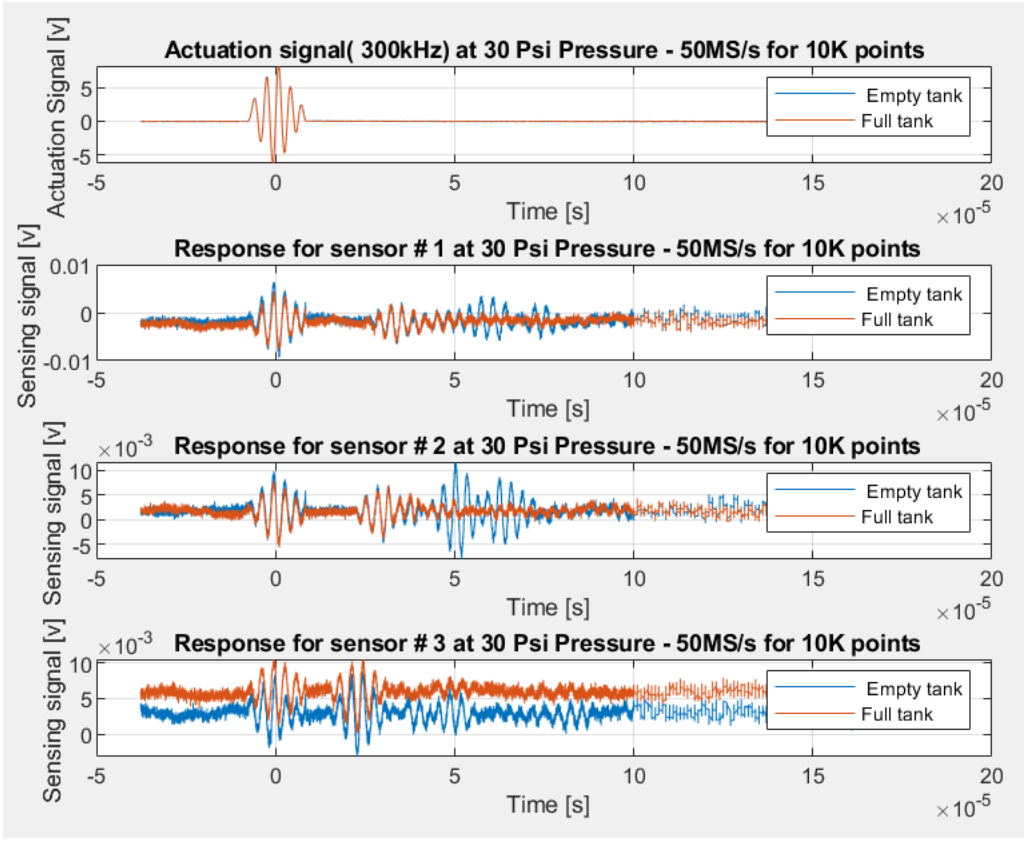

Figure 4.20: Comparison in sensor responses with empty and full tank at 30 psi.

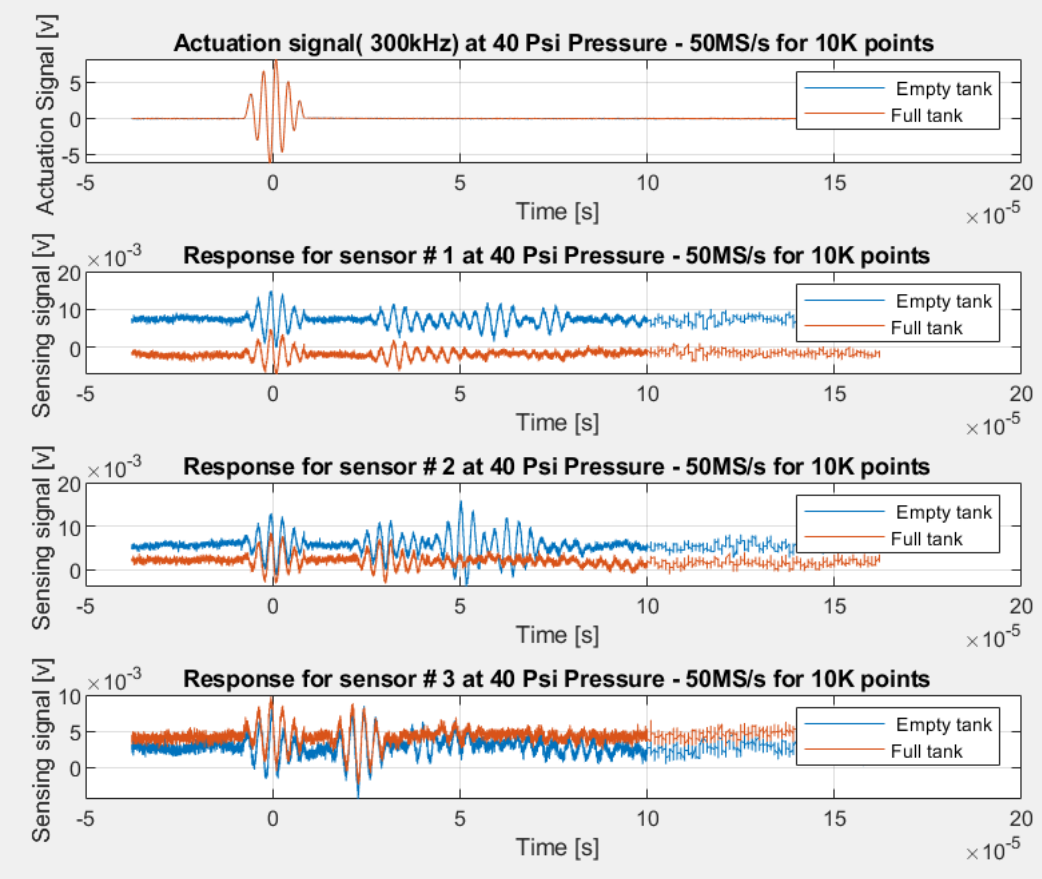

Figure 4.21: Comparison in sensor responses with empty and full tank at 40 psi.

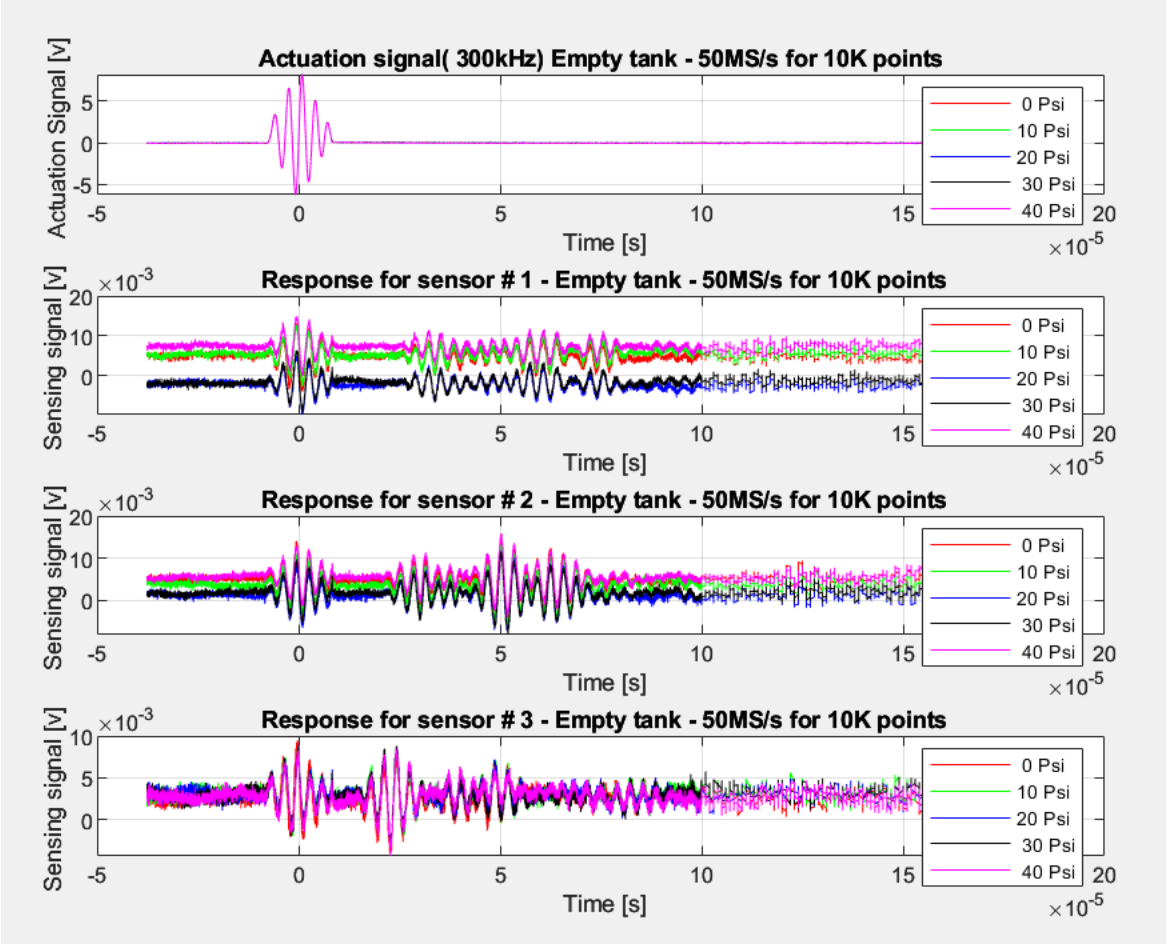

Figure 4.22: Comparison in sensor responses with an empty tank at different pressures

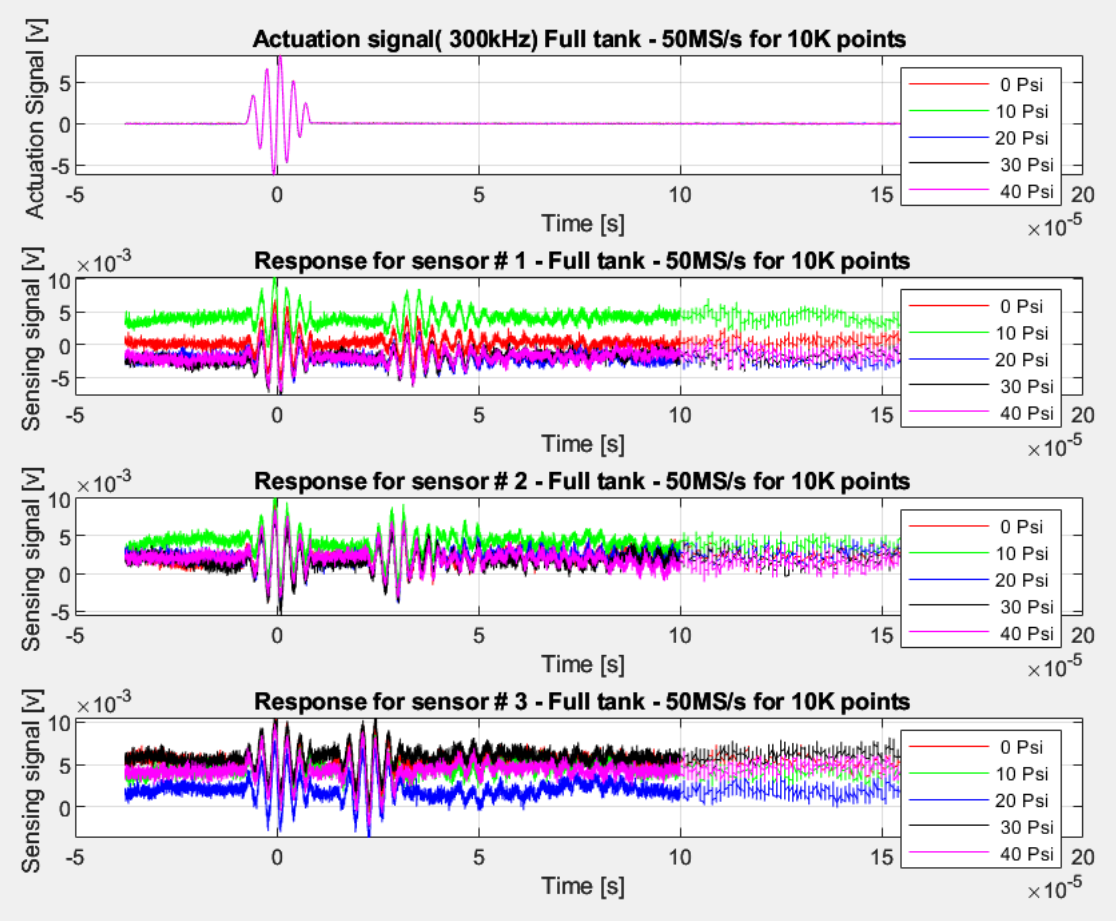

Figure 4.23: Comparison in sensor responses with a full tank at different pressures.

The sensing signal in the empty and full tank conditions was compared graphically at each of the four pressure conditions. Across each of the three pressure conditions, there is a significant drop in the signal arrival after the first wave packet for the full tank and this is true for each of the three sensing signals. The first wave packet arrival, symmetric node, is still present and the second wave packet, the antisymmetric node, has diminished greatly and is not seen graphically in **Figures 4.17-4.21**. Relating this to the theoretical background, the symmetric mode propagates in tension and compression where the antisymmetric mode operates in bending or flexural. Therefore, the symmetric mode continues to propagate quickly in the full tank and the

antisymmetric mode is dependent on changes to the surface of the material as the wave energy of the antisymmetric mode is dissipated when the tank is full.

In the comparison of the tank condition at varying pressures in **Figures 4.22** and **4.23** it is shown that the amplitude of the first wave packet is reduced as the pressure is increased and there is no difference in the ToF. It is difficult to view this graphically with the low amplitude actuation signal used because the voltage amplifier cannot be used. Below in **Figure 4.24** with trials from the full tank, the first at 0 psi and the second at 40 psi.

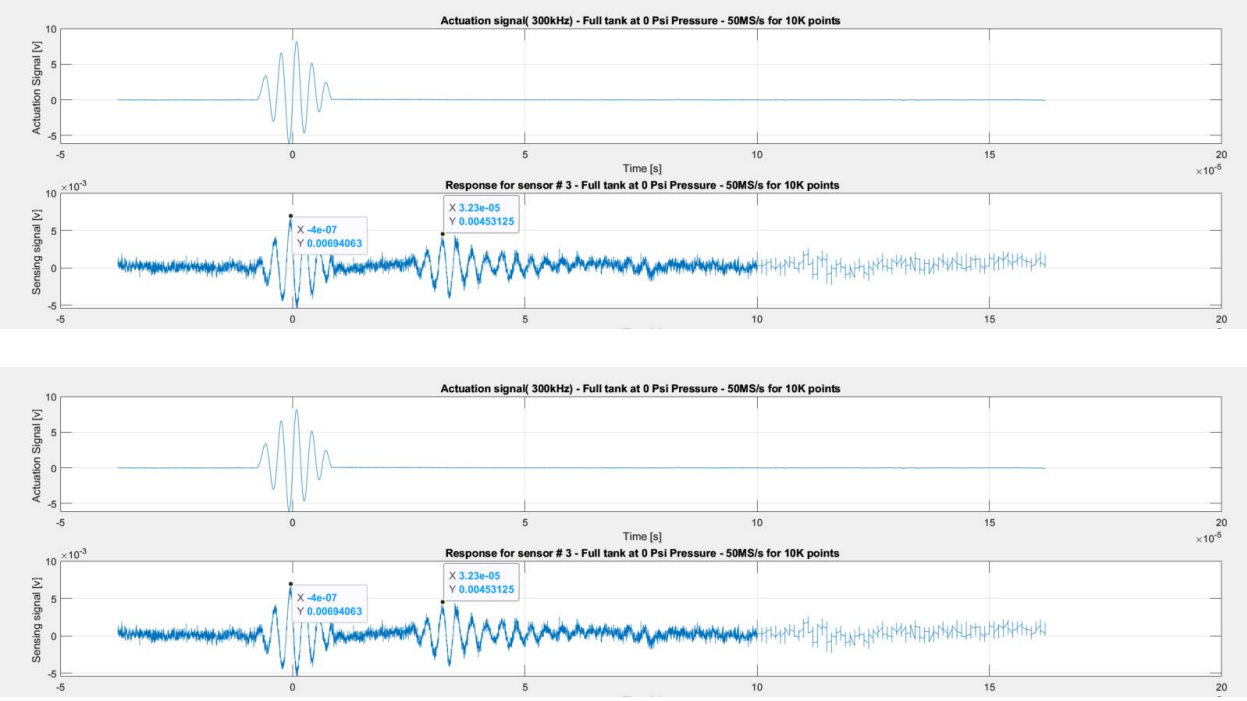

Figure 4.24: Comparison of sensor response in full tank at 0 and 40 psi. with peak amplitudes marked.

The second peak of the signal and response for sensor position 3 is marked to compare the amplitude. At 0 psi the peak goes from 0.00694 V in the signal down to 0.00453 V in the first wave packet arrival. At 40 psi the peak goes from 0.0048 V in the signal down to 0.00195 V in the first wave packet arrival. This is a 0.00241 V reduction at 0 psi and 0.00284 reduction at 40 psi. Further testing can explore this when a voltage amplifier is implemented, and the actuation

signal is of greater magnitude to verify this change is a result of the changing pressure conditions and not random noise in the signal.

Chapter 5 Conclusions and Future Work

SHM and ultrasonic inspection techniques have a wide range of applications because there is a high sensitivity for a wide range of factors from changing pressure to complex structure geometry. Using techniques established for basic structures, the signal propagation in a complex pressurized water tank can be understood and characterized when the tank has simulated damage and is empty or full at different pressure levels. Further work with this complex pressure vessel will continue exploratory research to grow the understanding of signal propagation in the structure and how this can be used to identify and locate degradation on the tank. Implementation of this damage detection has significant potential to increase the safety and reliability of a structure. Damage to a structure could be identified early and the damaged structure replaced or fixed before the whole system goes down and potentially causes more damage. The inspection process also has the potential to become automated to further the impact on saving time and resources in inspection and maintenance. Further work has the potential to research how this would be adapted to suit the needs of many fields and applications with the possibility to shape the future of automated inspection processes.

Chapter 6 Works Cited

1. F. K. Chang, “Structural Health Monitoring,” Hoboken, NJ, USA: Wiley, 2014.

2. S. Chandrasekaran, Structural Health Monitoring with Application to Offshore Structures. World Scientific, 2019.

3. V. M. Karbhari, “Structural Health Monitoring of Civil Infrastructure Systems,” Hoboken, NJ, USA: John Wiley & Sons, Inc., 2011.

4. C. R. Farrar and K. Worden, “Structural Health Monitoring: A Machine Learning Perspective,” Hoboken, NJ, USA: John Wiley & Sons, Inc., 2012.

5. R. B. Chase and A. Y. Steenberg, “Importance of Structural Health Monitoring and Immediate Feedback Systems for Civil Infrastructure,” in 2012 Structures Congress, 2012, pp. 379-390, doi: 10.1061/9780784412329.038.

6. H. Rocha, “Sensors for process and structural health monitoring of aerospace composites: A review,” Measurement Science and Technology, vol. 24, no. 2, p. 022001, Feb. 2013, doi: 10.1088/0957-0233/24/2/022001.

7. Z. He, W. Li, H. Salehi, H. Zhang, H. Zhou, and P. Jiao, “Integrated structural health monitoring in bridge engineering,” Structural Control and Health Monitoring, vol. 26, no. 1, p.e2441, Jan. 2019, doi: 10.1002/stc.2441.

8. A. Güemes, A. Fernandez-Lopez, A. R. Pozo, and J. Sierra-Pérez, “Structural Health Monitoring for Advanced Composite Structures: A Review,” Sensors, vol. 20, no. 17, p. 4827, Sep. 2020, doi: 10.3390/s20174827.

9. C. R. Farrar and K. Worden, An Introduction to Structural Health Monitoring. Oxford, UK: Butterworth-Heinemann, 2007.

10. D. L. Hunt, S. P. Weiss, W. M. West, T. A. Dunlap, and S. Freesmeyer, “Development and implementation of a shuttle modal inspection system,” in Proceedings of the IEEE Aerospace Conference, Big Sky, MT, USA, Mar. 1990, pp. 171-176, doi: 10.1109/AERO.1990.53697.

11. F. N. Catbas, M. Gul, and J. L. Burkett, “Damage assessment using flexibility and flexibility-based curvature for structural health monitoring,” Smart Materials and Structures, vol. 18, no. 12, p. 125008, Dec. 2009, doi: 10.1088/0964-1726/18/12/125008.

12. C. R. Farrar, H. Sohn, and G. H. Park, “A statistical pattern recognition paradigm for structural health monitoring,” Journal of Sound and Vibration, vol. 252, no. 3, pp. 529-544, 2002, doi: 10.1006/jsvi.2001.4138.

13. H. Sohn, C. R. Farrar, N. F. Hunter, and K. Worden, “Structural Health Monitoring Using Statistical Pattern Recognition Techniques,” Journal of Dynamics Systems, Measurement, and Control, vol. 123, no. 3, pp. 384-393, Sep. 2001, doi: 10.1115/1.1385984.

14. E. Figueiredo and J. Brownjohn, “Three decades of statistical pattern recognition paradigm for SHM of bridges,” Structure and Infrastructure Engineering: Maintenance, Management, Life-Cycle Design and Performance, vol. 12, no. 10, pp. 1156-1177, Oct. 2016, doi: 10.1080/15732479.2015.1060510.

15. F.-G. Yuan, S. A. Zargar, Q. Chen, and S. Wang, “Machine learning for structural health monitoring: challenges and opportunities,” Journal of Civil Structural Health Monitoring, vol. 10, no. 3, pp. 437-464, Jun. 2020, doi: 10.1007/s13349-020-00418-y.

16. Y. Bao and H. Li, “Machine learning paradigm for structural health monitoring,” Mechanical Systems and Signal Processing, vol. 100, pp. 439-461, Dec. 2017, doi: 10.1016/j.ymssp.2017.04.017.

17. P.W.R. Beaumont, C. Soutis, and A. Hodzic (Eds.), "Structural Integrity and Durability of Advanced Composites: Innovative Modelling Methods and Intelligent Design," Woodhead Publishing, Sawston, UK; Cambridge, UK, 2015, ISBN 978-0-08-100137-0.

18. P.B. Nagy, "Ultrasonic detection of kissing bonds at adhesive interfaces," J. Adhes. Sci. Technol., vol. 5, pp. 619-630, 1991.

19. T. Kundu, A. Maji, T. Ghosh, and K. Maslov, "Detection of kissing bonds by Lamb waves," Ultrasonics, vol. 35, pp. 573-580, 1998.

20. C. Ramadas, K. Balasubramaniam, M. Joshi, and C.V. Krishnamurthy, "Numerical and experimental studies on propagation of A0 mode in a composite plate containing semi-infinite delamination: Observation of turning modes," Compos. Struct., vol. 93, pp. 1929-1938, 2011.

21. B. Masserey, C. Raemy, and P. Fromme, "High-frequency guided ultrasonic waves for hidden defect detection in multi-layered aircraft structures," Ultrasonics, vol. 54, pp. 1720-1728, 2014.

22. K. Zhang and Z. Zhou, "Quantitative characterization of disbonds in multilayered bonded composites using laser ultrasonic guided waves," NDT E Int., vol. 97, pp. 42-50, 2018.

23. N. Guo and P. Cawley, "Lamb wave propagation in composite laminates and its relationship with acousto-ultrasonics," NDT E Int., vol. 26, pp. 75-84, 1993.

24. C. Ramadas, K. Balasubramaniam, M. Joshi, and C.V. Krishnamurthy, "Characterisation of rectangular type delaminations in composite laminates through B- and D-scan images generated using Lamb waves," NDT E Int., vol. 44, pp. 281-289, 2011.

25. R. Dugnani, Y. Zhuang, F. Kopsaftopoulos, and F.-K. Chang, "Adhesive bond-line degradation detection via a cross-correlation electromechanical impedance-based approach," Struct. Health Monit., vol. 15, pp. 650-667, 2016.

26. Y. Zhuang, Y.-H. Li, F. Kopsaftopoulos, and F.-K. Chang, "A self-diagnostic adhesive for monitoring bonded joints in aerospace structures," in Proceedings of the Sensors and Smart Structures Technologies for Civil, Mechanical, and Aerospace Systems, Las Vegas, NV, USA, 20 April 2016.

27. V. Giurgiutiu, “Electromechanical Impedance-Based Structural Health Monitoring,” Morgan & Claypool Publishers, 2007.

28. S. Guo, Q. Sun, and T. Lu, “Electromechanical Impedance of Piezoelectric Structures and Materials,” Academic Press, 2019.

29. H. Altammar, A. Dhingra, and N. Salowitz, “Damage detection using D15 piezoelectric sensors in a laminate beam undergoing three-point bending,” Smart Materials and Structures, vol. 17, no. 3, p. 035018, May 2008, doi: 10.1088/0964-1726/17/3/035018.

30. P. Kudela, W. Ostachowicz, and A. Żak, "Damage detection in composite plates with embedded PZT transducers," IEEE Transactions on Ultrasonics, Ferroelectrics, and Frequency Control, vol. 54, no. 10, pp. 2072-2084, October 2007. DOI: 10.1109/TUFFC.2007.507.

31. H. Lamb, “On Waves in an Elastic Plate,” The Royal Society. [Online]. Available: https://royalsocietypublishing.org/doi/10.1098/rspa.1917.0008

32. V. Giurgiutiu, *Structural Health Monitoring with Piezoelectric Wafer Active Sensors*. Oxford: Academic Press, an imprint of Elsevier, 2014.

33. X. Liu, C. Zhou, and Z. Jiang, "Damage Localization in Plate-Like Structure Using Built-In PZT Sensor Network," Sensors, vol. 16, no. 11, article no. 1899, Nov. 2016, doi: 10.3390/s16111899.

34. "Root mean squared deviation is". Brainly, from https://brainly.in/question/34450056

35. Coding Prof. (2022, January). 3 Ways to Calculate the Mean Absolute Percentage Error in R [Examples]. CodingProf.com. Jan. 2022, from https://www.codingprof.com/3-ways-to-calculate-the-mean-absolute-percentage-error-in-r-examples/

36. A. Antoniadis, S. T. Quek, and J. Y. Shi, "Nonlinear Ultrasonic Techniques for Damage Detection and Imaging," Journal of Nondestructive Evaluation, vol. 35, no. 2, pp. 34, 2016, doi: 10.1007/s10921-016-0361-3.

37. "CircuitWorks Conductive Epoxy Technical Data Sheet", Ladd Research https://www.laddresearch.com/lanotattachments/download/file/id/249/store/1/60802.pdf

38. J. L. Rose, "Dispersion of Ultrasonic Waves in Solids," Journal of Materials Science, vol. 34, no. 15, pp. 3371-3381, Aug. 1999, doi: 10.1023/A:1004631423783.

39. R. Johnson and E. Williams, "A Manual Approach to Peak Frequency Analysis in Time-Domain Signals," in IEEE Transactions on Signal Processing, 2018.

40. R. L. Allen and D. W. Mills, "Signal Analysis: Time, Frequency, Scale, and Structure," John Wiley & Sons, 2004.

41. M. Demetriou, "Practical Signal Analysis for Scientists and Engineers," CRC Press, 2018.

42. S. W. Smith, "Power Spectral Density Estimation Using the Welch Method," in IEEE Signal Processing Magazine, vol. 14, no. 6, pp. 76-80, Nov. 1997, doi: 10.1109/79.641758.

43. J. Cohen, "An Introduction to the Welch Method of Power Spectral Density Estimation," in 2014 IEEE International Conference on Acoustics, Speech and Signal Processing (ICASSP), pp. 7084-7088, May 2014, doi: 10.1109/ICASSP.2014.6854969.

44. H. L. Van Trees, "Spectrum Analysis: A Modern Perspective," Prentice Hall, 2002.

45. C. H. Chen and C. H. Liu, "Chirp-Z Transform: Algorithm, Implementation, and Applications," in IEEE Transactions on Signal Processing, vol. 49, no. 9, pp. 2163-2177, Sep. 2001, doi: 10.1109/78.942614.

46. Z. Wu, N. E. Huang, and S. R. Long, "Chirp Parameter Estimation via Empirical Mode Decomposition," in IEEE Transactions on Signal Processing, vol. 55, no. 5, pp. 2283-2291, May 2007, doi: 10.1109/TSP.2006.889188.

47. S. Zhang, H. Huang, and J. Song, "A Chirp-based Method for Estimating the Instantaneous Frequency of a Signal," in IEEE Signal Processing Letters, vol. 22, no. 8, pp. 1120-1124, Aug. 2015, doi: 10.1109/LSP.2014.2383621.

48. J. Takatsubo and Y. Fujino, "Effect of Natural Frequency on Ultrasonic Guided Wave Propagation in Pipe Structures," Journal of Sound and Vibration, vol. 267, no. 3, pp. 679-694, Jul. 2003, doi: 10.1016/S0022-460X(02)01524-3.

49. L. H. Thostrup, M. R. Geiker, K. L. Olsen, and M. A. Lacasse, "Natural Frequencies and Mode Shapes of Ultrasonic Wave Propagation in Concrete," Journal of Applied Geophysics, vol. 57, no. 2, pp. 157-171, Jun. 2005, doi: 10.1016/j.jappgeo.2004.11.005.

50. P. Avanesians and M. Momayez, "Wave separation: Application for arrival time detection in ultrasonic signals," Ultrasonics, vol. 55, pp. 15-25, 2015. DOI: 10.1016/j.ultras.2014.08.019.

51. J. Hou, K. R. Leonard, and M. K. Hinders, "Automatic multi-mode Lamb wave arrival time extraction for improved tomographic reconstruction," in IEEE Transactions on Ultrasonics, Ferroelectrics, and Frequency Control, vol. 65, no. 4, pp. 612-621, Apr. 2018, doi: 10.1109/TUFFC.2017.2789321.

Chapter 7 Bibliography

Trevor Wenzel was born in Sheboygan, Wisconsin, April 27th, 2000. He obtained his Bachelor of Science in Mechanical Engineering from the University of Wisconsin - Milwaukee in December of 2021 and began a Master's in Engineering with a concentration in Mechanical Engineering the following semester at the University of Wisconsin – Milwaukee in the spring of 2022 with an expected graduation in the spring of 2023. He currently works as an Engineer I with Generac Power Systems in Waukesha, Wisconsin working with the industrial generator team in product development and design. Work projects include enclosure analysis for extreme loading conditions of high wind and snow applications as well as thermal analysis of engine exhaust temperatures to create effective heat shielding around turbocharger systems. Previously, he worked as a Sustainability Engineering Intern with Sargento Inc. developing the sustainability program through an analysis of the power usage trends and performance as well as recycling and trash-to-landfill projects. He performed undergraduate research with the University of Wisconsin – Milwaukee Bicycle and Motorcycle Engineering Research Laboratory in the 2020-2021 academic year working to design and implement a tilt control and user interface for a three wheeled recumbent tricycle. In his graduate studies he is currently working in the Advanced Structures Laboratory at the University of Wisconsin – Milwaukee exploring ultrasonic pressure vessel damage detection using a network of piezoelectric sensors. Outside of the classroom, he competes as a member of the University of Wisconsin – Milwaukee's track and cross country team setting multiple school records from 5000m to 10,000m and volunteering for community events like the Milwaukee Make a Difference Day and Milwaukee Marathon.

Chapter 8 Appendix: Actuation signal and sensor responses for empty and full tank at 0, 10, 20, 30, and 40 psi.

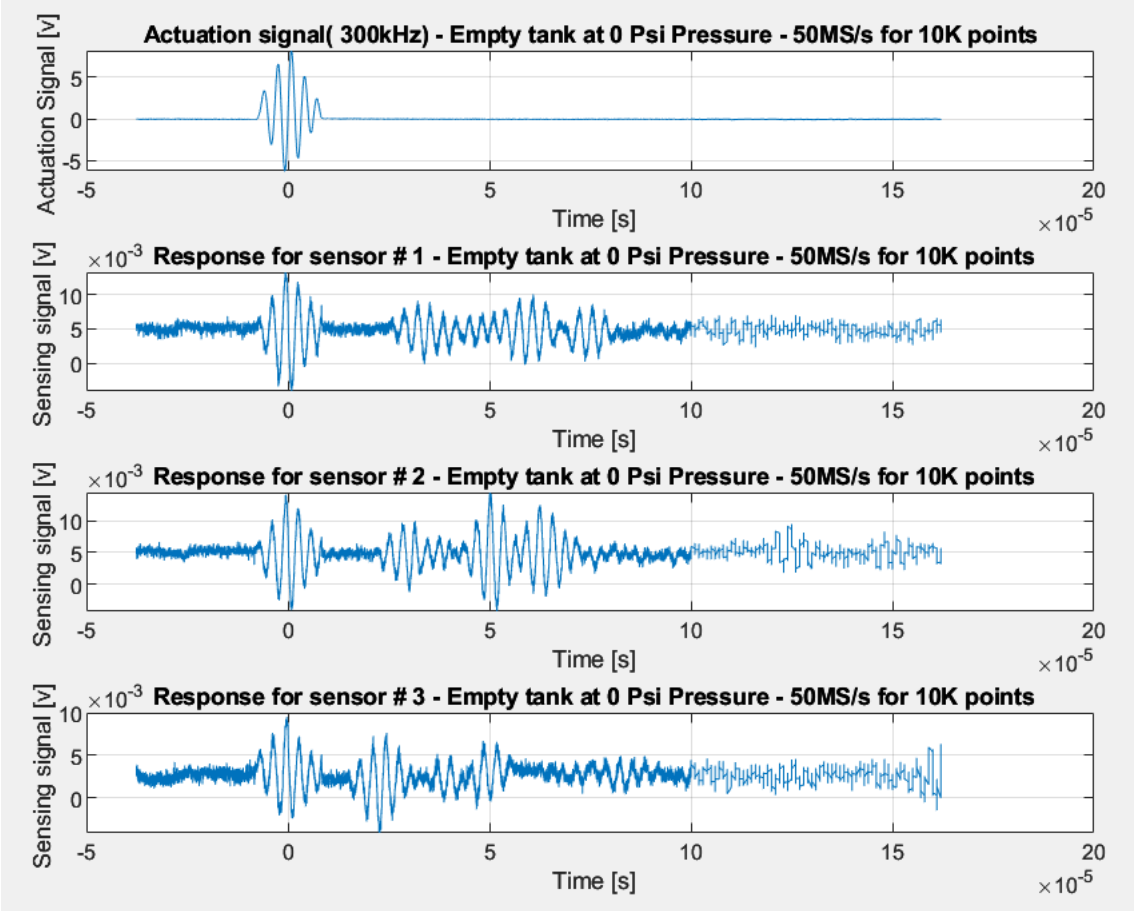

Figure 8.1: Actuation signal and sensor responses with empty tank at 0 psi.

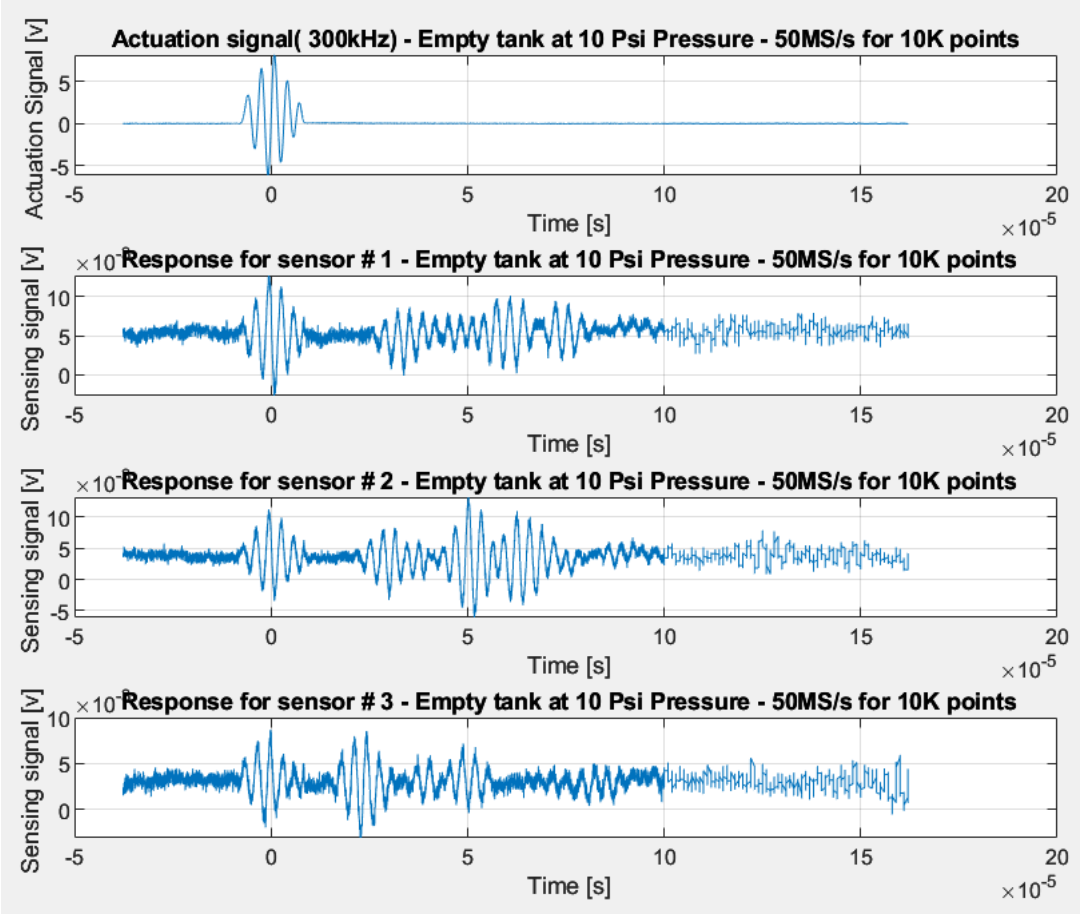

Figure 8.2: Actuation signal and sensor responses with empty tank at 10 psi.

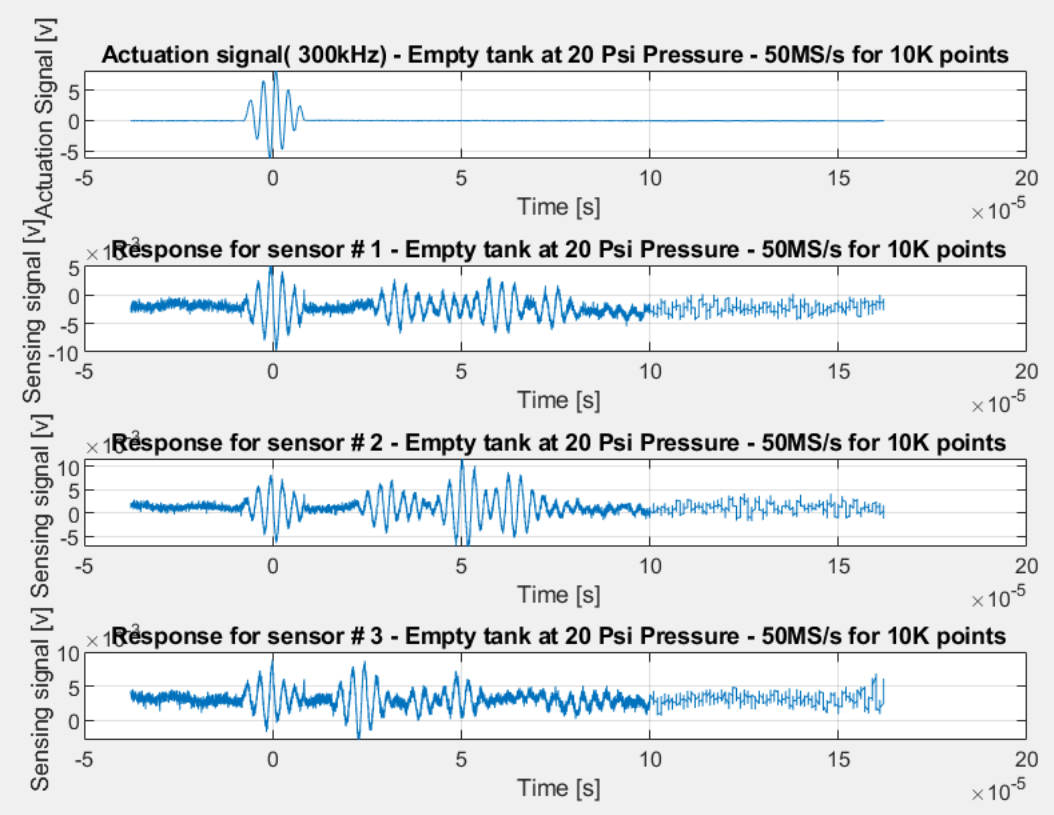

Figure 8.3: Actuation signal and sensor responses with empty tank at 20 psi.

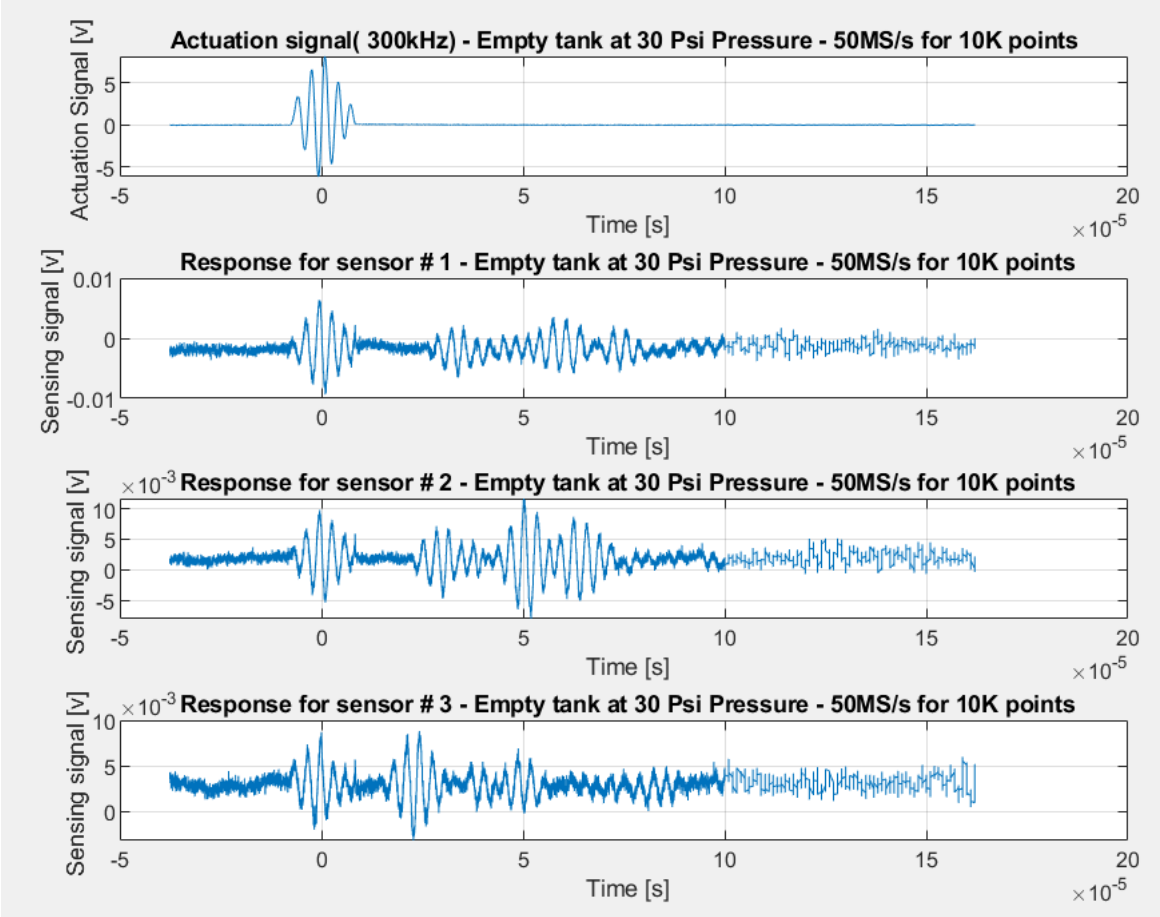

Figure 8.4: Actuation signal and sensor responses with empty tank at 30 psi.

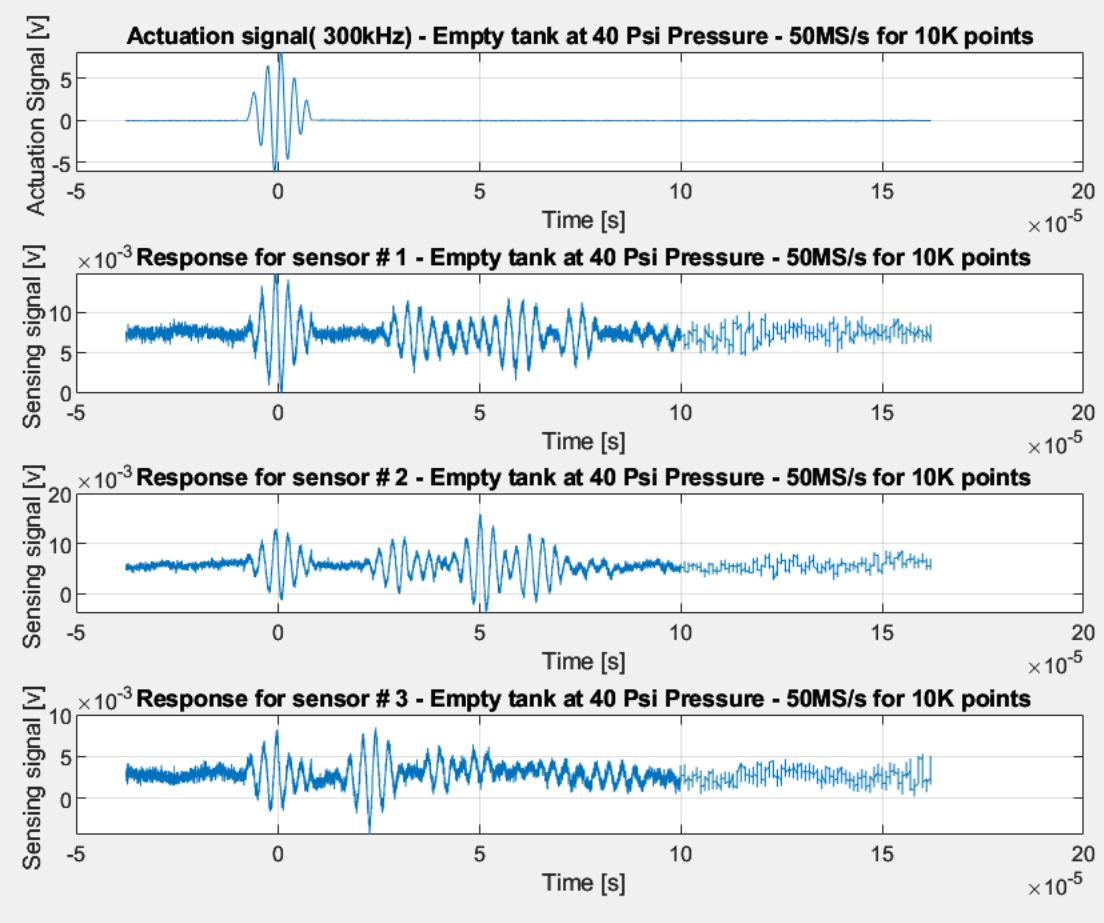

Figure 8.5: Actuation signal and sensor responses with empty tank at 40 psi.

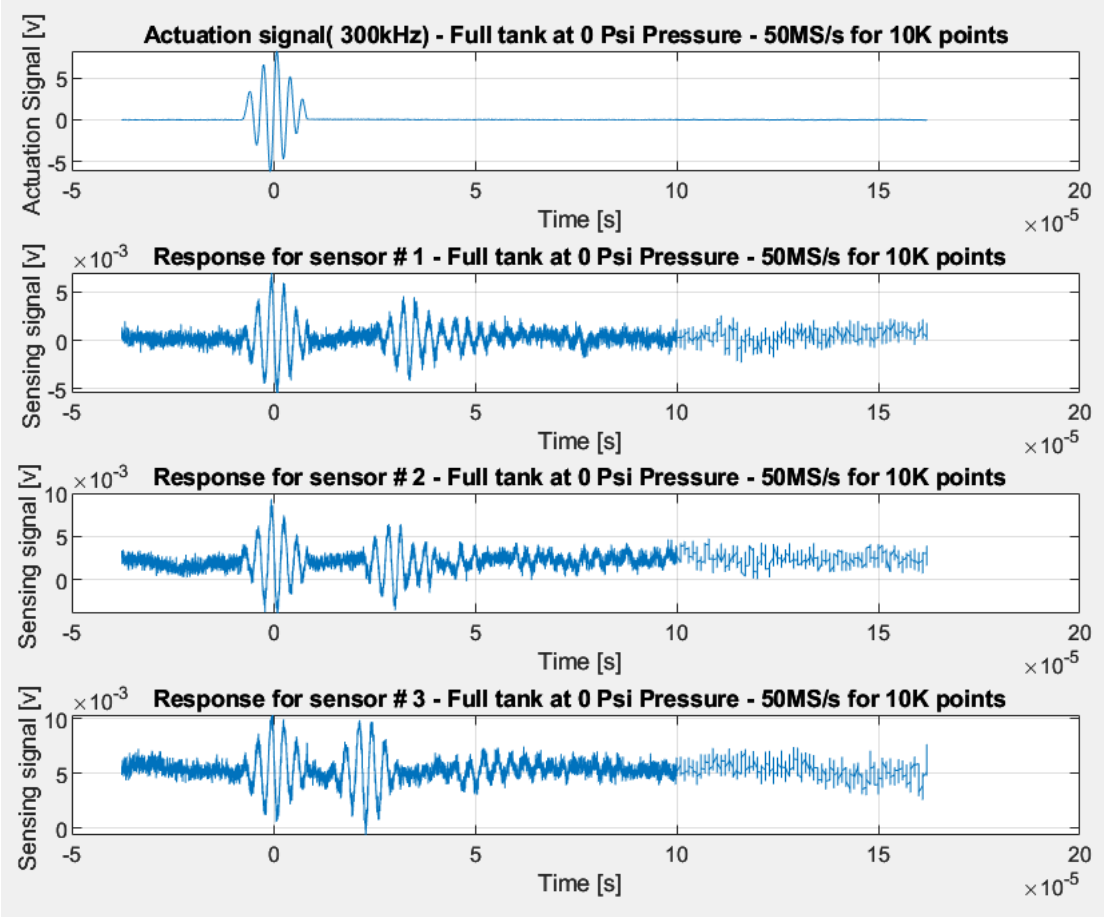

Figure 8.6: Actuation signal and sensor responses with full tank at 0 psi.

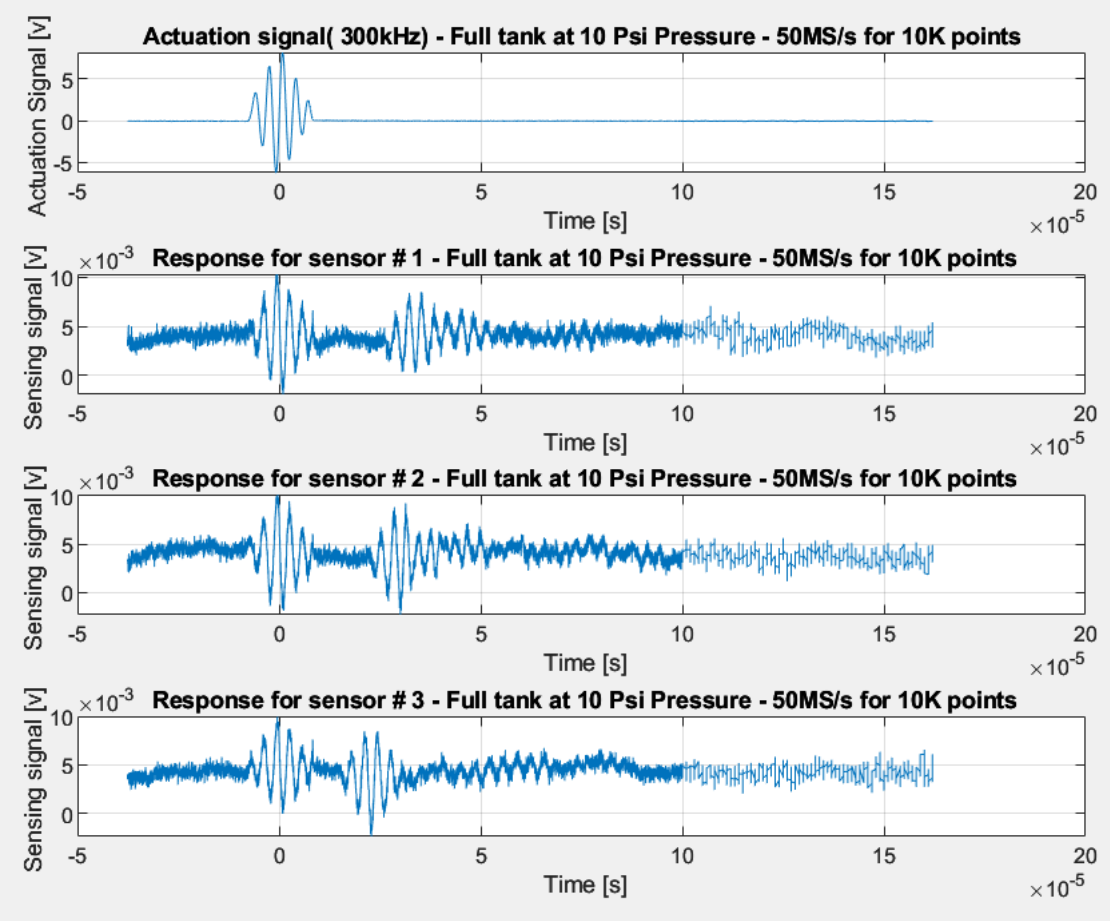

Figure 8.7: Actuation signal and sensor responses with full tank at 10 psi.

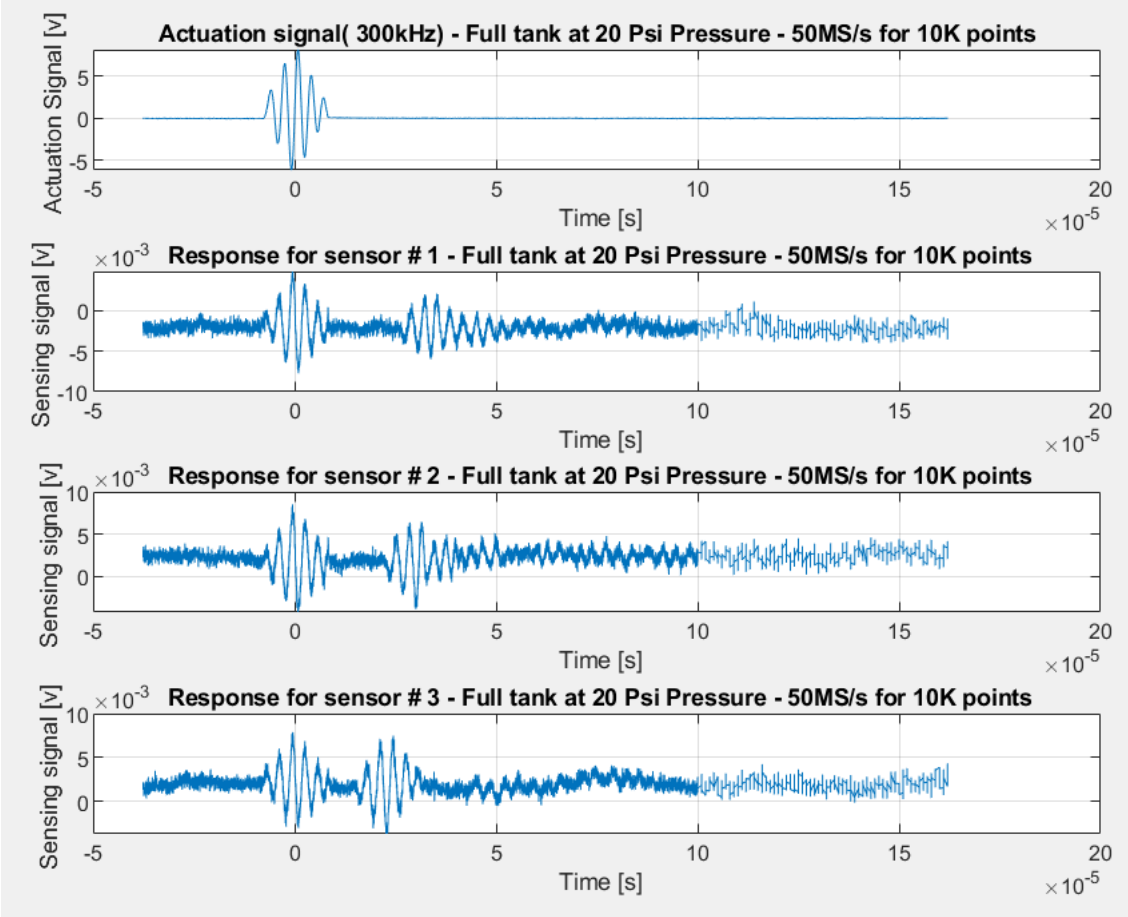

Figure 8.8: Actuation signal and sensor responses with full tank at 20 psi.

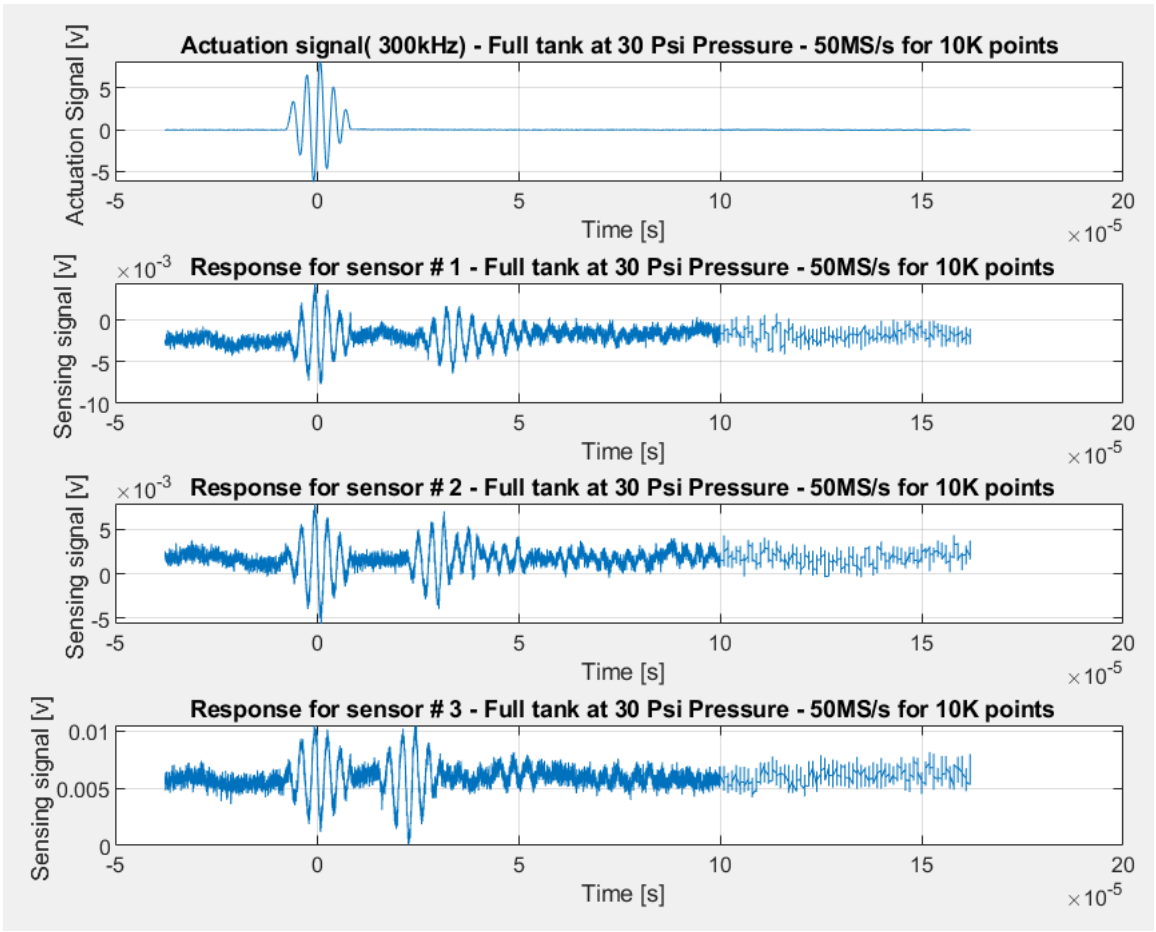

Figure 8.9: Actuation signal and sensor responses with full tank at 30 psi.

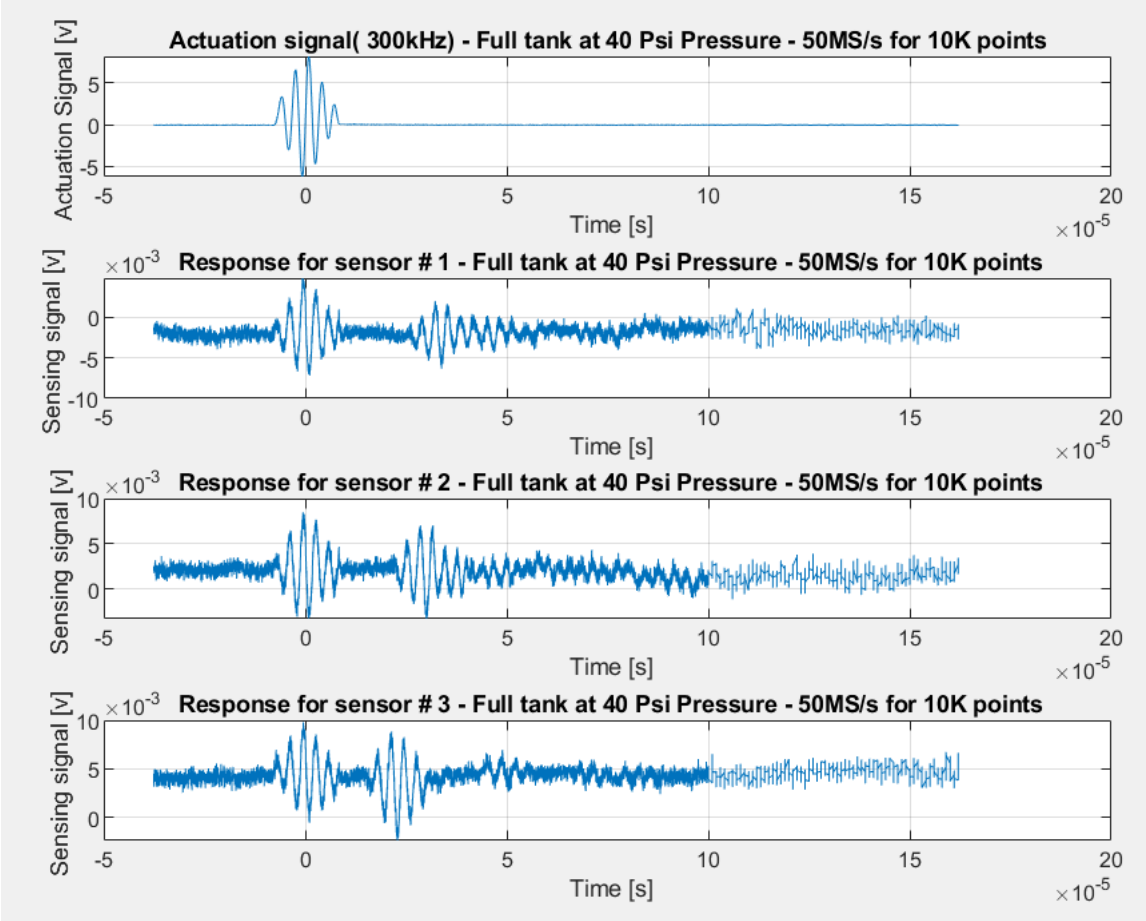

Figure 8.10: Actuation signal and sensor responses with full tank at 40 psi.